PNL-4623
UC-94e

DISCLAIMER

PHYSICAL MODELING OF THE CHAMPAGNE EFFECT

PNL--4623

DE84 001813

P. A. Thompson
H. J. Sneck
B. Hand
B. Meyer
C. Ping
E. Roehl
Rensselaer Polytechnic Institute
Troy, New York

September 1983

Prepared for
the U.S. Department of Energy
under Contract DE-AC06-76RLO 1830

Pacific Northwest Laboratory
Richland, Washington 99352

PACIFIC NORTHWEST LABORATORY PERSPECTIVE

Compressed air energy storage (CAES) is a technique for supplying electric power to meet peak load requirements of electric utility systems. Using low-cost power from base load plants during off-peak periods, a CAES plant compresses air for storage in an underground reservoir--an aquifer, solution-mined salt cavity, or mined hard rock cavern. During subsequent peak load periods, the compressed air is withdrawn from storage, heated, and expanded through turbines to generate peak power. This relatively new technology offers significant potential for reducing costs and improving efficiency of electric power generation, as well as reducing petroleum fuel consumption.

Based on these potential benefits, the U.S. Department of Energy (DOE) is sponsoring a comprehensive program to accelerate commercialization of CAES technology. The Pacific Northwest Laboratory (PNL) was designated the lead laboratory for the CAES Program. As such, PNL is responsible for assisting the DOE in planning, budgeting, contracting, managing, reporting, and disseminating information. Under subcontract to PNL are a number of companies, universities, and consultants responsible for various research tasks within the program.

An important element of this program is to investigate phenomena that may be detrimental in the commercialization of CAES. One such concern is the "champagne effect". It is thought that the champagne effect may occur in a hydraulically-compensated hard rock cavern when air, dissolved in the water by diffusion through the air-water interface, rises to the surface with an increasing air volume fraction due to deaeration of water and decompression of the air in the decreasing pressure field. This process has the potential to cause a loss of cavern pressure or even blowout of the cavern.

This report documents an investigation conducted by the Department of Mechanical Engineering at Rensselaer Polytechnic Institute. The study's purpose was twofold: to determine the factors that influence the formation

of bubbles in a CAES cavern and to develop a mathematical model capable of predicting the effect of those bubbles on the discharge of water from a cavern. The findings presented herein contribute substantively to the growing understanding of the champagne effect phenomenon and its role in CAES cavern operation.

Landis D. Kannberg, Manager
Underground Energy Storage Program
September 1983

SUMMARY

Successful commercialization of compressed air energy storage (CAES) technology depends largely on the ability to understand and predict potentially detrimental aspects of its implementation. A particularly important concern is the "champagne effect", a hydraulic process with the potential to cause a loss of storage cavern pressure or even blowout of the cavern. Under subcontract to the Pacific Northwest Laboratory, researchers at Rensselaer Polytechnic Institute conducted an investigation to determine the factors that influence bubble formation in a CAES cavern. Using this information, they then undertook to develop a model to predict the effect of those bubbles on the discharge of water from a CAES cavern.

This research project involved parallel analytical and experimental efforts. Two physical models were developed, one relatively simple and analytical, the other much more detailed and numerical. A high-solubility carbon dioxide/water laboratory model of a CAES system was also constructed. Results obtained from bubble formation experiments using the laboratory-scale CAES facility were compared with those generated by the predictive models.

The high-solubility CO_2/H_2O champagne effect laboratory model successfully simulated the behavior of a CAES system. Researchers noted that varying conditions of heterogeneous nucleation in bulk produced profound differences in the vigor of the observed champagne effect. Experimental observations further suggest that reproducible heterogeneous nucleation experiments are possible. The simple analytical model was found to show excellent agreement with the detailed numerical model. The latter, in turn, showed good agreement with the data obtained experimentally in the laboratory-scale CAES facility. Researchers concluded that physical modeling is relevant to practical studies of the champagne effect, and that the results of such modeling should be used in designing future experiments.

ACKNOWLEDGMENTS

The authors would like to acknowledge the advice and support of Dr. Walter V. Loscutoff and Dr. Landis D. Kannberg of the Pacific Northwest Laboratory and of several of their colleagues there.

Several individuals have made valuable contributions to the project while they were students at Rensselaer Polytechnic Institute, in particular, Brian Hand, Ker-Lin Pei, Chen Ping, Edwin Roehl and Bruce Meyer.

CONTENTS

FIGURES

TABLES

NOMENCLATURE

A	shaft cross-sectional area
$\bar{A}$	nondimensional area, A/A_0
A_b	bubble surface area
a	gas-liquid interfacial surface area per unit volume
C	nondimensional inverse soundspeed squared
C_L	inlet loss coefficient
c	speed of sound
c_e	equilibrium speed of sound
c_f	frozen speed of sound (c_e when concentration of dissolved gas is constant)
D	compensation shaft diameter, diameter
D^*	nondimensional shaft diameter, D/D_0
$\mathcal{D}$	diffusion coefficient
d	bubble diameter
d_{nuc}	effective diameter of bubble nucleus
F	nondimensional spatial pressure gradient, see Equation (62)
f	Darcy friction factor
f_s	bubble friction factor
$f'(Y)$	axial transformation spatial gradient, see Equation (57)
G	Nondimensional spatial gas-liquid fraction gradient, see Equation (63)
G_i^n	discretized mixture mass flux term
g	gravitational acceleration
g_y	vertical component of gravitational acceleration

$\underline{g}$ gravitational acceleration vector

H plant head, difference in water level between surface and underground reservoirs

h_b U-bend depth

K mass transfer coefficient

L compensation shaft length (including U-bend)

Mg molecular weight of gas

M_ℓ molecular weight of liquid

m mass

$\dot{m}$ mass flow rate

$\bar{m}$ relative velocity exponent

n Schmidt exponent, see Equation (46)

n_b number density of active nucleation sites

P nondimensional pressure, P/Pa

P_a nondimensional atmospheric pressure, $Pa/\rho_\ell u_o^2$

P_c nondimensional concentration pressure, P_c/P_a

p pressure

p_f wetted perimeter

p_o cavern pressure

$\dot{q}$ volumetric flow rate

R gas constant

$R^n_{i+1/2}$ discretized momentum flux term

RG^n_i discretized total gas mass flux term

RV^n_i discretized vapor mass flux term

r bubble radius

$\bar{r}$ equilibrium mean bubble radius

S slip ratio, u_g/u_ℓ

Sc Schmidt number, $\nu_\ell/\mathcal{D}$

Sh Sherwood number, $Kd/\mathcal{D}$

S_i discretized source rate term

T temperature

T* period of oscillation

t time

t_H Helmholtz resonator period

t_o characteristic time

U nondimensional velocity, u/u_o

U_o constant, nondimensional liquid velocity at start of compensation column, where V = 0

u velocity

$\underline{u}$ velocity vector

u_r relative velocity, $u_g - u_\ell$

u_t terminal rise velocity

V volume of gas per unit volume liquid, V_g^*/V_ℓ^*

$\bar{V}$ cube root of gas-liquid fraction, $V^{1/3}$

V* volume

V_b^* bubble volume

V_c^* cavern volume

V_{ea} equilibrium gas-liquid fraction at top of column

X nondimensional distance

Y nondimensional height, y/H

y position on axis of compensation shaft

Z nondimensional axial transformation coordinate, Z = f(Y)

Greek Symbols

α	void fraction, V_g^*/V_t^*
β	angle with horizontal
Γ	source rate
γ	ratio of specific heats (gas)
γ_1-γ_2	nondimensional parameters, see Equation (56)
γ_1^*,γ_5^*	nondimensional parameters, see Equation (86)
ΔY	nondimensional mesh spacing
Δy	mesh spacing
$\Delta\bar{\rho}$	nondimensional density difference
δ	incremental operator
$\delta\tau$	nondimensional time step size
δZ	nondimensional mesh spacing
ϵ	relative error or tolerance
η_1	degree of saturation
η_2	degree of pressurization
θ	time weighted mass constant
Λ	Henry's constant
$\bar{\Lambda}$	ambient nondimensional concentration, Λp_a
$\bar{\Lambda}_c$	nondimensional concentration, Λp_c
λ	nondimensional Henry's constant
μ	dynamic viscosity
ν	kinematic viscosity
π_e	Euler number
π_f	dimensionless friction number
π_g	inverse Froude number

π_h dimensionless head number

π_m dimensionless mass transfer number

π_r Reynolds number

π_s dimensionless solubility number

π_u Strouhal number

π_1, π_2 coefficients defined in Equation (56)

ρ density

ρ_g total gas density (bubble and dissolved)

ρ_v vapor density, p/RT

ρ^* flow density, $\frac{\alpha\rho_v S}{1-\alpha} + \rho_\ell(1 + \Delta p_c)$

$\bar{\rho}$ nondimensional density, p/ρ_ℓ

σ surface tension

τ nondimensional time, $u_o t/H$

τ_w wall shear stress

ϕ time weighted pressure constant

ψ angle between $\underline{u}$ and $\underline{g}$

ω nondimensional factor relating void fraction and number density of active nucleation sites

ω^* over/under relaxation parameter

Subscripts

a atmospheric

a/w air-water system

b bubble, bend

c concentration, cavern

c/w CO_2 - water system

eq	equilibrium
g	gas
ga	gage
gb	gas in bubble
gℓ	gas dissolved in liquid
i	finite difference mesh index
ℓ	liquid
m	mixture, mixed mean
o	inlet, initial, or reference
p	pipe, pressure
r	relative, reference
t	total, tank, terminal rise
v	vapor
y	coordinate direction
∞	infinite medium

Superscripts

^	beginning of iteration value
~	after iteration value
‾	nondimensional
n	explicit in time
n+1	implicit in time

PHYSICAL MODELING OF THE CHAMPAGNE EFFECT

1.0 INTRODUCTION

Peaking power demands are now met by utilities primarily through the use of combustion turbines, which have an established technology and relatively low capital cost. The increasing cost of oil and gas, however, has tended to offset the capital benefit-cost ratios of these installations. Consequently, utilities are seeking alternative sources of peak load generation that efficiently use their off-load generation installed capacity during off-load periods to store energy. Energy storage systems transfer the excess energy from base load units generated during periods of low demand.

One of the most promising candidates for energy storage is the compressed air energy storage (CAES) system. A CAES system consists of an underground cavern containing the pressurized air and sealing water, a compensating U-tube joining the cavern to ground-level holding pond, and an air compressor/turbine, which can be coupled to the primary power generating source. This system is attractive because, for the most part, its major components use existing technologies such as tunneling and turbine and compressor construction. Its relatively small size and underground location make it economically and environmentally attractive as well.

For all of its advantages, potential problem areas have been identified. One of these is the "champagne effect", which may occur in the compensating U-tube that seals the system from the ambient pressure. During the cavern charging process, the cavern water is forced up the compensating shaft of the U-tube. When this water reaches the upper levels of the shaft where the local pressure is less than the saturation pressure of the air in water solution, air bubbles will form. If substantial quantities of air are released, the density of this two-phase mixture could be considerably less than that of the water, thereby reducing the sealing

capacity of the fixed height column. The result could be a loss-of-pressure accident during which a large portion of the cavern water would be rapidly discharged upward through the compensating column with severe consequences.

This investigation was conducted by Rensselaer Polytechnic Institute (RPI) to determine the factors influencing the formation of bubbles and to develop a predictive model to describe their effect on the discharge of water from the cavern. The work reported here results from a parallel analytical and experimental program performed for the Pacific Northwest Laboratory (PNL). Two physical models were developed, one relatively simple and analytical, the other much more detailed and numerical. A high solubility laboratory model of the CAES system was also constructed. The experimental results obtained from this facility were correlated with those generated by the predictive models. These aspects of this research program are documented in this report. In addition, several fundamental unanswered questions requiring further investigation are identified and methods for their resolution suggested.

2.0 CONCLUSIONS AND RECOMMENDATIONS

The work described here was concluded more than a year after the expiration of financial support. This report thus provides an opportunity to give impressions of the significance of our work and comments on champagne-effect research generally.

2.1 CONCLUSIONS

The RPI work included physical modeling, simple analytical modeling, numerical modeling, and high-solubility champagne-effect experiments. The following conclusions are drawn with respect to these efforts:

1. Physical modeling is relevant to practical studies of the champagne effect. The results of such modeling should be used in the design of experiments.
2. The simple analytical model presented here shows excellent agreement with the detailed numerical model, which in turn shows good agreement with the limited experimental data available. The simple analytical model is of value to validate computer calculations and to identify important effects.
3. Varying conditions of heterogeneous nucleation in bulk produce profound differences in the vigor of the observed champagne effect. Experimental observations suggest that reproducible heterogeneous nucleation experiments are possible.
4. A better understanding of the nucleation process is fundamental to the development of a fully predictive CAES model.
5. The high-solubility CO_2/water champagne effect model has functioned about as anticipated and simulates the behavior of a CAES system.

2.2 RECOMMENDATIONS

In September 1982, some information became available at the AIAA/EPRI International Conference on Underground Pumped Hydro and Compressed Air

Energy Storage on results from other studies of the champagne effect. This included numerical modeling (Giramonti, Blecher and Smith 1982; Pellin 1982) and reports on experiments (Pellin 1982; Rowe and McMonagle 1982; Ruzich and Miller 1982). The planned Soyland CAES plant (Vann and Freezor 1982) which will make use of hydraulic compensation, was also extensively described. Two very expensive full-scale champagne-effect experiments, with estimated costs of $3.6 million and $3.0 million, were proposed for mine sites.

Much of the reported and continuing work appears to be of value. For future champagne effect work, we would offer four recommendations:

1. Large-scale computer programs for prediction of the champagne effect should be tested against actual, relevant experiments and simple calculations.
2. Experimental results should be shared openly, consistent with the safety and reliability issues involved in the champagne effect.
3. A reduced atmospheric pressure air/water model should be considered as a realistic and far less expensive alternative to full-scale mine testing.
4. Nucleation and gas release problems should be adequately and cooperatively addressed.

3.0 PHYSICAL MODELING OF THE CHAMPAGNE EFFECT

The "physical modeling" in terms of nondimensional parameters has two uses: it permits a rational mathematical description in terms of a minimum number of parameters and it allows accurate experimental modeling by means of a relatively small-scale model system. An example of a nondimensional parameter in fluid mechanics is the Reynolds number $\pi_r = Du_o\rho/\mu$; an example of experimental physical modeling is the model test of reversible hydraulic pump/turbines.

The need for scale-model experiments is evident from the application relevant to this work: large-scale compressed air energy storage (CAES) in subterranean hard rock at approximately 1000 m below the surface of the earth. An experimental facility with a compensation shaft of this height can be assumed to cost almost as much as the CAES plant itself--hundreds of millions of dollars. A scale-model experiment is thus desirable.

The dimensional parameters expected to play a role in the champagne effect in a CAES system appear in the Nomenclature. Among the most important are plant head H, defined as the difference in water level between the surface and underground reservoirs; gas-in-liquid solubility represented by Henry's constant Λ; compensation shaft diameter D; cavern volume V_c^*; liquid density ρ_ℓ; liquid viscosity μ; surface tension σ; mass transfer coefficient K; cavern pressure p_o; atmospheric pressure p_a; pumping velocity u_o; molecular weight of the gas Mg; characteristic time t_o; and the acceleration of gravity g. There are several additional parameters.

Before discussing the nondimensional groups essential to physical modeling, it is useful to discuss the nature of the gas dissolution in terms of Henry's Law,

$$m_{g\ell} = m_\ell \Lambda p \tag{1}$$

where $m_{g\ell}$ is the equilibrium value of the mass of gas dissolved in the liquid, m_ℓ the mass of liquid, p the static pressure and $\Lambda = \Lambda(T)$ is

Henry's constant, which depends strongly on the particular gas-liquid combination: concisely stated, the equilibrium concentration of dissolved liquid is proportional to pressure.[a]

The amount of gas released from solution into bubbles, i.e., the dissolution, determines the vigor of the champagne effect. Under equilibrium conditions, the total mass of gas released into bubbles m_{gb} is given by, from Equation (1)

$$\frac{m_{gb}}{m_\ell} = \Lambda(p_o - p_a) \approx \Lambda \rho_\ell g H \qquad (2)$$

The ratio of the volume of gas to the volume of liquid will be this value multiplied by the density ratio ρ_ℓ/ρ_g at atmospheric pressure. Supposing for the moment that this density ratio is constant, the nondimensional parameter $\Lambda\rho_\ell gH$ is the principal measure of the strength of the champagne effect.

This parameter is mainly governed by the product ΛH of solubility and head. In our experimental modeling, we have sought a gas-liquid system for which Λ would be large, permitting a scale model in which the head H takes on a manageable value. For the air/water system in a CAES plant, Henry's constant Λ at 20°C is $\Lambda_{a/w} = 2.4 \cdot 10^{-5}$ kg/kg-bar (Kruis 1976; Emmerich, Battino, and Wilcock 1976) and the head is in the order of $H = 10^3$ m. To model the Equation (2) parameter with a head of (say) 10^1 m, it is only necessary to find a gas-liquid system for which Henry's constant is greater than $\Lambda_{a/w}$ by a factor of 10^2. Referring to Kruis (1976), one finds gas-liquid systems for which Λ is greater by as much as a factor of 10^4. For various practical reasons, we finally chose a CO_2/water system (C/W) for which $\Lambda_{c/w} = 71\ \Lambda_{a/w}$ at 20°C. An exact modeling calculation (accounting for differences in gas density) then yields a scale experimental model head of H = 21.5 m.

[a] For the systems of interest here, nonlinear corrections to Henry's Law play a minor role (Kruis 1976).

3.1 NONDIMENSIONAL PARAMETERS

Starting from the dimensional parameters listed at the beginning, one can form nondimensional groups in various ways. A suitable choice for the most important groups π_i is the following:

$$
\begin{aligned}
&1. \quad \pi_h \equiv \rho_\ell g H / p_a && \text{head} \\
&2. \quad \pi_s \equiv \Lambda \rho_\ell R T && \text{solubility} \\
&3. \quad \pi_f \equiv fH/2D && \text{friction} \\
&4. \quad \pi_m \equiv \frac{\omega \rho_\ell D u_o}{6kH} && \text{mass transfer} \\
&5. \quad \pi_r \equiv \rho_\ell D u_o / \mu && \text{Reynolds number} \\
&6. \quad \pi_e \equiv p_a / \rho_\ell u_o^2 && \text{Euler number} \\
&7. \quad \pi_g \equiv gH/u_o^2 && \text{inverse Froude number} \\
&8. \quad \pi_u \equiv H/u_o t_o && \text{Strouhal number}
\end{aligned}
\tag{3}
$$

There are, of course, additional groups such as the Weber number. The parameter f in π_f is the Darcy friction factor. The nondimensional factor ω in π_m is related to the number density n_b of active nucleation sites in the liquid by

$$\omega^3 = 6/n_b \pi D^3 \tag{4}$$

as discussed later. Alternatively, ω can be determined from the experimental local bubble diameter d and void fraction α from

$$\omega^3 = \frac{1-\alpha}{\alpha} \left(\frac{d}{D}\right)^3 \tag{5}$$

and is of order unity in many situations. Its value may depend on the cleanliness of the liquid, a point which will be considered in subsequent sections.

The product $\pi_h\pi_s$ of the nondimensional head and the solubility is the equilibrium value of the ratio V_{ea} of gas volume to liquid volume at the top of the compensation column,

$$V_{ea} = \left(\frac{\rho_\ell gH}{p_a}\right)\left(\Lambda\rho_\ell RT\right) = \pi_h\pi_s \tag{6}$$

[The volume ratio V is related to void fraction α by $V = \alpha/(1-\alpha)$]. The equilibrium volume ratio for a 1000-m prototype CAES system is about 1.95. Any physical model chosen should, at least, reproduce the value V_{ea} of Equation (6).

3.2 CANDIDATE EXPERIMENTAL MODELS FOR A CAES PROTOTYPE

The only experimental system that can reproduce every aspect of the prototype CAES air/water system is the CAES system itself. Next, in order of fidelity to the prototype, appear to be the following systems:

1. low-pressure atmosphere model using air and water or nitrogen and water (π_h, π_s, π_f, π_m, π_r, can be modeled, the latter approximately)
2. low-pressure atmosphere model using other gas/liquid combinations ($\pi_h\pi_s$, π_f, π_m, π_r)
3. standard-pressure atmosphere model using high-solubility gas liquid combinations ($\pi_h\pi_s$, π_f, π_r).

The first two model types require a closed system with an exhaust pump to maintain a low-pressure atmosphere above the surface reservoir; they are more complicated and much more expensive than the third type. Table 3.1 lists possible design parameters for the three types of model systems. Only one of the models is exact in the sense discussed above.

3.3 MODELING OF UNSTEADY FLOW

Much of the concern about the champagne effect in CAES plants centers on flow transients associated with starting and stopping the charge and

TABLE 3.1. Possible Experimental Model Systems

Type	Gas/ Liquid	M_g	M_ℓ	ρ_ℓ	$\Lambda_{20°C}$	H	p_a/p_o	Note
		$\frac{g}{mol}$	$\frac{g}{mol}$	$\frac{kg}{m^3}$	$\frac{kg}{kg\text{-}bar}$	m	bar	
Prototype	air	28.97	18.02	997.0	$2.4 \cdot 10^{-5}$	1000.0	1.013	
	water						98.80	
Low Pressure Atmosphere	air	28.97	18.02	997.0	$2.4 \cdot 10^{-5}$	40.0	0.0405	
	water						3.951	
	CF_4	88.01	671.10	1901.0	0.00200[a]	6.30	0.634	(b)
	PFTBA						1.809	
	CO_2	44.01	46.07	789.3	0.0070	8.46	1.013	(b)
	C_2H_5OH						1.668	
Standard Pressure Atmosphere	CO_2	44.01	18.02	997.0	0.0172	21.5	1.013	(b)
	water						3.115	
	CO_2	44.01	18.02	997.0	0.00172	9.96	1.013	(b),(c)
	water						1.986	

NOTES: (a) This value is from Powell (1972).
(b) π_h not modeled, but $\pi_h \pi_s$ is modeled.
(c) Models H = 460 m prototype.

discharge of the underground air caverns. The potentially resulting oscillatory flow may be usefully compared to that in a classical Helmholtz resonator, with liquid in the compensation column forming the oscillating mass and the pressurized air caverns forming the spring. The period t_H of this Helmholtz resonator is

$$t_H = 4\sqrt{\frac{\pi \rho_\ell L V_c^*}{\gamma p_o D^2}} \tag{7}$$

where $L \sim H$ is the total length of the compensation shaft (including U-bend) and γ is the ratio of specific heats for the gas. The effective cavern volume V_c^* can vary considerably, of course: V_c^* is intended to represent the actual volume of air in the caverns. Additional nondimensional parameters can then be formed by dividing by other characteristic times, in particular H/u_o and the startup or shutdown time (ramp time) of turbomachinery. These additional parameters, such as π_u, can also be experimentally modeled.

3.4 REYNOLDS NUMBER

The Reynolds number π_r depends mainly on the viscosity μ of the liquid, the characteristic pumping velocity u_o and the diameter of the compensation shaft. If u_o is taken to be the velocity induced by a full-dissolution champagne effect, the Reynolds number for the prototype system in Table 3.1 is $\sim 10^8$; for the experimental systems listed it is $\sim 10^5$ to 10^6. For typical pumping velocities with no champagne effect, π_r would be approximately an order of magnitude smaller.

4.0 SIMPLE ANALYTICAL MODEL

Relatively simple equations for the champagne effect in the compensation shaft can be found if the flow is treated as one-dimensional, isothermal, without interphase slip and without bubble coalescence or fractionation. For a vigorous champagne effect, these equations are more or less realistic and have the advantage of being understandable. The inaccuracies associated with this model are perhaps less significant than those associated with incomplete understanding of nucleation and supersaturation.

The model is conceptually based on a hypothetical fixed mass of liquid m_ℓ and an associated fixed mass of gas m_g, initially fully dissolved in the liquid (Figure 4.1). In the following, we consider conservation of liquid and conservation of gas. The pure liquid phase is assumed to have constant density ρ_ℓ and to undergo no volume change due to solution or dissolution of gas. For simplicity, we neglect the change in density of the liquid

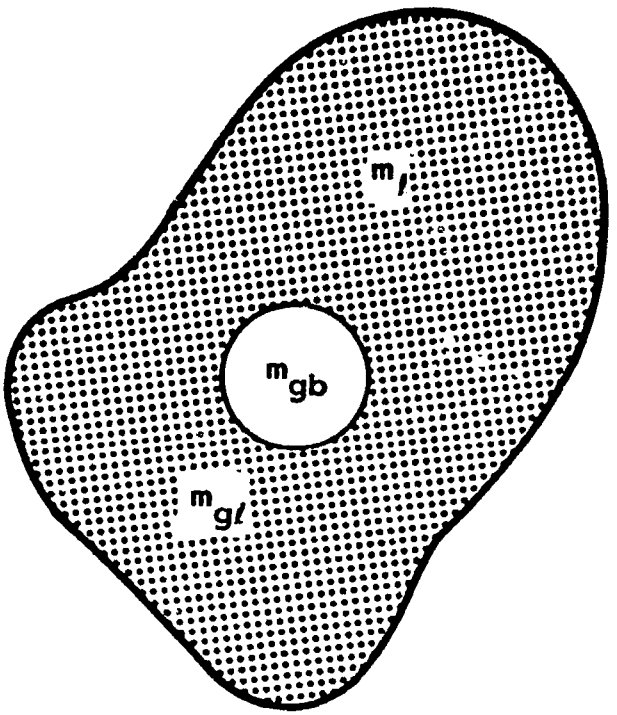

FIGURE 4.1. Conceptual Illustration of the Fixed Liquid Mass with Associated Bubble and Mass of Gas

phase due to solution or dissolution (this corresponds to the assumption $\Lambda p_o << 1$) and equivalently, that the mass of gas is negligible compared to the mass of liquid.

Let the volume ratio V be the volume of gas per unit volume of liquid. This is formally related to the usual void fraction α by

$$V = \alpha/(1-\alpha) \tag{8}$$

From conservation of liquid, the average density ρ of the two-phase mixture is related to V by

$$\frac{\rho}{\rho_\ell} = \frac{1}{V + 1} \tag{9}$$

and the perfect-gas law yields

$$\frac{m_{gb}}{m_\ell} = \frac{pV}{\rho_\ell RT} \tag{10}$$

The total mass of gas m_g is assumed to be in equilibrium solution in the liquid at reservoir pressure p_o; this mass is divided into m_{gb} in the bubble and $m_{g\ell}$ dissolved in the liquid,

$$m_{gb} + m_{g\ell} = \Lambda p_o m_\ell \tag{11}$$

Let the actual concentration of gas in the liquid be represented by the concentration pressure p_c. Thus, $m_{g\ell} = \Lambda p_c m_\ell$ and for the special case of equilibrium (Henry's law) concentration, $p_c = p$. Equation (11) yields

$$m_{gb} = \Lambda(p_o - p_c)m_\ell \tag{12}$$

The mass transfer to the bubble is driven by the concentration difference $p_c - p$ with an overall mass transfer coefficient $K\Lambda$: the rate of bubble growth is then

$$\frac{dm_{gb}}{dt} = A_b K\Lambda(p_c - p) \tag{13}$$

where A_b is the surface area of the bubble. The application of an overall coefficient K implies that resistance to mass transfer by diffusion is

neglible, i.e., that the liquid is well-stirred, or turbulent. Combining Equations (12) and (13) to eliminate p_c yields

$$\frac{m_{gb}}{m_\ell} + \frac{1}{A_b K}\frac{dm_{gb}}{dt} = \Lambda(p_o - p) \tag{14}$$

which reduces to Henry's law in the form of Equation (12) when mass transfer vanishes and $p = p_c$.

We now introduce a scaling hypothesis, that the bubble volume is proportional to the volume fraction V. This is equivalent to assuming that a bubble, once formed, neither coalesces with another bubble, nor fractionates into other bubbles and that all bubbles can be represented (at a point in space and time) by an effective bubble diameter d. Thus,

$$V_b^* = \text{const. } V \tag{15}$$

Writing the constant as $\omega^3 \pi D^3/6$, where D is the compensation shaft diameter, this becomes

$$d^3 = \omega^3 D^3 V \tag{16}$$

The constant ω depends on the number n_b of active nucleation sites per unit volume. Setting $d = d_{nuc}$ and $V = n_b \pi d_{nuc}^3/6$ yields

$$\omega^3 = \frac{6}{n_b \pi D^3} \tag{17}$$

Even with the aid of devices such as particle counters, however, it is difficult to determine n_b directly. A practical alternative is to determine ω (and thus n_b) by measuring bubble diameter d and volume ratio V at any point in the flow, i.e., ω is supposed to be invariant for any given flow.

4.1 EQUATIONS OF MOTION

The three equations required are those for conservation of mass, conservation of momentum and mass transfer. The three dependent variables (unknowns) may be taken to be pressure, velocity and volume ratio.

The one-dimensional, constant-area pipe-flow equations for mass and momentum are, respectively,

$$\frac{\partial \rho}{\partial t} + \frac{\partial}{\partial y}(\rho u) = 0 \tag{18}$$

$$\rho \frac{\partial u}{\partial t} + \rho u \frac{\partial u}{\partial y} + \frac{\partial p}{\partial y} = -\frac{f \rho u^2}{2D} \sin(u) + \rho g \cos\psi \tag{19}$$

where the velocity u is considered positive in the +y direction and ψ is the angle between the velocity vector $\underline{u}$ and the gravity (acceleration) vector $\underline{g}$. The y-axis lies along the axis of the compensation shaft. The mass-transfer equation is Equation (14).

Putting Equations (18), (19), and (14) in nondimensional form yields the following three equations:

$$\frac{\partial}{\partial \tau}\left(\frac{1}{V+1}\right) + \frac{\partial}{\partial Y}\left(\frac{U}{V+1}\right) = 0 \tag{20}$$

$$\frac{\partial U}{\partial \tau} + U \frac{\partial U}{\partial Y} + \frac{\pi_e}{V+1} \frac{\partial P}{\partial Y} = -\pi_f U^2 \sin(U) + \pi_g \cos\psi \tag{21}$$

$$PV + \pi_m V^{-2/3}\left(\frac{\partial}{\partial \tau} + U \frac{\partial}{\partial Y}\right) PV = \pi_s(\pi_h + 1 - P) \tag{22}$$

where the nondimensional independent and dependent variables are

$$\tau \equiv u_o t/H \qquad U \equiv u/u_o$$

$$Y \equiv y/H \qquad V \equiv \rho_\ell/\rho - 1$$

$$P \equiv p/p_a$$

4.2 STEADY-FLOW EQUATIONS

For steady flow, the continuity equation reduces to

$$U = U_o(V + 1) \tag{23}$$

where U_o is a constant, the nondimensional liquid velocity at the start of the compensation shaft where $V = 0$. Using this, the remaining equations (21, 22) can be reformed into two equations, each of which contains only one first-order derivative,

$$(V + 1)\left[\pi_e P - U_o^2 V\right]\frac{\partial P}{\partial Y} = U_o^2 \bar{V}^2 A_1 - P B_1 \tag{24}$$

$$3(V + 1)\left[\pi_e P - U_o^2 V\right]\frac{\partial V}{\partial Y} = \pi_e A_1 + \bar{V} B_1 \tag{25}$$

where $V \geq 0$ and

$$A_1 \equiv \frac{\pi_s(\pi_h + 1) - P(\pi_s + V)}{\pi_m U_o}$$

$$B_1 \equiv \pi_f U_o^2 (V + 1)^2 - \pi_g \cos\psi$$

$$\bar{V} \equiv V^{1/3}$$

The function $\pi_e P - U_o^2 V$ represents a determinant of coefficients from the original equations and will be represented by the symbol C_1.

Comments on these equations, as they relate to the champagne effect, follow. The function A_1 vanishes for equilibrium values of $V(P)$, as can be seen by setting the derivative to zero in Equation (22), is positive for supersaturation and negative for undersaturation.

Consider the upward flow in the ascending (long) leg of the compensation shaft during the charging cycle of the CAES plant. Near the bottom of the U-bend, the volume ratio will be zero,[(a)] i.e., the liquid will be undersaturated and A_1 will be negative. Both B_1 and C_1 will be positive.

As the liquid moves up the shaft, the pressure decreases and the function A_1 turns positive at some point: saturation is followed by supersaturation, $\partial\bar{V}/\partial Y > 0$, and bubbles begin to grow. With increasing

(a) Neglecting the volume of the nucleation sites. These sites must, of course, survive the overpressure in order for a champagne effect to take place.

height Y the pressure P continues to decrease (from gravity, friction and acceleration) and the volume ratio $V = \bar{V}^3$ continues to increase. If this process were to continue, the coefficient C_1 would become zero and Equations (24) and (25) could be satisfied only by making the derivatives $\partial P/\partial Y$ and $\partial \bar{V}/\partial Y$ infinite.

This behavior is typical of gasdynamic choking, as encountered, for example, in duct flow with friction or heat transfer. The limiting velocity is the speed of sound c. In the present problem, there are two soundspeeds: the equilibrium soundspeed c_e is defined by

$$c_e^2 \equiv (\partial p/\partial \rho)_{p=p_c} \tag{26}$$

that is, the concentration of the gas in the liquid is the equilibrium value specified by Henry's law. The frozen soundspeed c_f is given by

$$c_f^2 \equiv (\partial p/\partial \rho)_{p_c=\text{const}} \tag{27}$$

that is, the concentration of gas in the liquid remains constant. In both Equations (26) and (27) the temperature T is assumed constant. The required relation for $p(\rho)$ is found from Equations (10) and (12),

$$V = \pi_s \frac{p_o - p_c}{p} \tag{28}$$

with p_c set either to p or a constant, as required, together with Equation (9). Differentiation then yields

$$c_e^2 = \frac{p}{\rho_\ell} \frac{(V+1)^2}{V + \pi_s} \tag{29}$$

$$c_f^2 = \frac{p}{\rho_\ell} \frac{(V+1)^2}{V} \tag{30}$$

It is the "frozen" soundspeed corresponding to Equation (30) which governs the choking limit in Equations (24), and (25). Let u_o be the liquid velocity at the bottom of the compensation shaft, where V = 0. Then setting $C_1 = 0$ in Equations (24) and (25) yields

$$\frac{p}{\rho_\ell u_o^2} = V \tag{31}$$

at the (real or hypothetical) section where choking obtains. Inserting this into Equation (30) yields

$$c_f^2 = u_0^2(V + 1)^2$$

and continuity gives the velocity at this section

$$u^2 = u_0^2(V + 1)^2$$

i.e., the Mach number based on c_f is unity.

5.0 DETAILED NUMERICAL MODELING

In this section, an analytical model is developed for analyzing gas dissolution/absorption in buoyancy/pressure driven multiphase flows in variable area channels. The equations describing the conservation of mass and momentum for gas, dissolved gas in solution and liquid are used to calculate velocities, void fraction, dissolved gas concentration and pressure as a function of time. Major assumptions are:

1. The flow is one-dimensional.
2. Gas and liquid temperatures are equal and constant.
3. Dissolved gas and liquid move at the same velocity.
4. Surface tension is negligible (equal gas and liquid pressure). Surface tension effects on nucleation can, however, be incorporated.
5. The multiphase mixture behaves as a Newtonian fluid.
6. Steady-state mass transfer conditions between the phases are established instantaneously with negligible gas-side mass transfer resistance.

5.1 UNSTEADY MIXTURE EQUATIONS OF CHANGE

The drift-flux field equations for the multiphase mixture consist of one momentum and three mass conservation equations. The mass conservation equations consist of mixture mass, vapor mass and total gas mass. The following forms of these four partial differential equations are:

Mixture Mass Conservation

$$\frac{\partial}{\partial t}\left[\rho_m\right] + \frac{1}{A}\frac{\partial}{\partial y}\left[\rho_m u_m A\right] = 0 \tag{32}$$

Vapor Mass Conservation

$$\frac{\partial}{\partial t}\left[\alpha\rho_v\right] + \frac{1}{A}\frac{\partial}{\partial y}\left[\alpha\rho_v u_m A\right] + \frac{1}{A}\frac{\partial}{\partial y}\left[\alpha\rho_v \frac{(1-\alpha)(1+\Lambda p_c)}{\rho_m}\rho_\ell u_r A\right] = \Gamma \tag{33}$$

Total Gas Mass Conservation

$$\frac{\partial}{\partial t}[\rho_g] + \frac{1}{A}\frac{\partial}{\partial y}[\rho_g u_m A] + \frac{1}{A}\frac{\partial}{\partial y}\left[\alpha\rho_v\left(1 - \frac{\rho_g}{\rho_m}\right)u_r A\right] = 0 \qquad (34)$$

Mixture Momentum Conservation

$$\frac{\partial}{\partial t}[\rho_m u_m] + \frac{1}{A}\frac{\partial}{\partial y}[\rho_m u_m^2 A] + \frac{1}{A}\frac{\partial}{\partial y}\left[\alpha\rho_v\left(1 - \frac{\alpha\rho_v}{\rho_m}\right)u_r^2 A\right] = -\frac{\partial p}{\partial y} - \rho_m g_y - \tau_w p_f/A \qquad (35)$$

where:

Mixture Density, $\rho_m \equiv (1 - \alpha)\rho_\ell(1 + \Lambda p_c) + \alpha\rho_v$

Total Gas Density, $\rho_g \equiv (1 - \alpha)(\Lambda p_c)\rho_\ell + \alpha\rho_v$

Mixture Velocity, $u_m \equiv \dfrac{(1 - \alpha)\rho_\ell(1 + \Lambda p_c)u_\ell + \alpha\rho_v u_g}{\rho_m}$ (36)

Relative Velocity between Phases, $u_r \equiv u_g - u_\ell$

5.2 CONSTITUTIVE RELATIONSHIPS

The four additional relationships needed for closure of the system of equations are referred to as constitutive equations. These include the equations of state for the liquid and vapor densities and saturation of dissolved gas (Henry's constant). The relative velocity, wall shear and vapor source term must also be specified for closure. General forms for these equations are now presented.

5.2.1 Equations of State

The equations of state for the density of the three constitutents are:

Liquid

$$\rho_\ell = \rho_\ell(T) \qquad (37)$$

Vapor

$$\rho_v = p/RT$$

5.2.2 Dissolved Gas (Saturated)

$$(\Lambda p_c)\rho_\ell = \Lambda(p,T)p\rho_\ell \tag{38}$$

where a constant temperature T has been assumed. The liquid is assumed incompressible with density a function of temperature only. The vapor density is defined by the ideal gas law where R is the gas constant. The density of dissolved gas, defined as the mass of dissolved gas per unit volume of liquid, is defined by Henry's law for a saturated liquid, where Henry's "constant" Λ is a function of pressure and temperature.

5.2.3 Source Term

The source term Γ represents the amount of gas dissolution/absorption per unit volume per unit time and is defined as

$$\Gamma = K a \rho_\ell [(\Lambda p_c) - \Lambda p] \tag{39}$$

where a is the gas-liquid interfacial surface area/unit volume, Λp_c is the dissolved gas mass/liquid mass, Λ is Henry's constant and p is the local system pressure. To include surface tension effects in the source term p must be replaced by $p - 2\sigma/r$. This will however have a negligible effect except at very small bubble radii.

The controlling two-phase mass transfer parameters depicted in the source term which govern the rate of gas dissolution/absorption are gas-liquid interfacial area per unit volume a and mass transfer coefficient K. An equivalent bubble radius model is also required since both of the mass transfer parameters are functions of bubble size.

Since the nucleation process is assumed to be heterogeneous, an initial interfacial gas-liquid surface area per unit volume is included for modeling the onset of nucleation. Other variations in mass transfer parameters are also possible to account for delayed nucleation or cavitation. This additional information, however, must be determined from experimental data and modeled into the constitutive relationships.

5.2.4 Interfacial Area

Expressions for the interfacial area per unit volume and void fraction as functions of bubble size and density can be represented, respectively, by

$$a = n_b 4\pi r^2 + a_o \tag{40}$$

and

$$\alpha = n_b \, 4/3\pi r^3 \tag{41}$$

where

$a_o = (n_b)_o 4\pi r_o^2$, initial interfacial area per unit volume on suspended particulates and channel wall at $\alpha = 0$

r = equivalent bubble radius

r_o = equivalent initial bubble radius (onset of nucleation)

n_b = total number of bubble/nucleation sites per unit control volume

$(n_b)_o$ = initial number of nucleation sites per unit volume on suspended particulates and channel wall (onset of nucleation)

Eliminating bubble density n_b from Equation (40) by algebraic substitution of Equation (41) yields

$$a = \frac{3\alpha}{r} + a_o \tag{42}$$

which is the governing interfacial area equation. For bulk nucleation from particulates (motes) with an initial radius r_o and blanketed by a gas-liquid film, the interfacial area can be represented by

$$a = \left(\frac{(n_b)_o 4\pi r_o^3 + 3\alpha}{r} \right) .$$

The equivalent bubble radius is assumed to be a function of void fraction. Equation (42) is generally applicable for all two-phase flow regimes, even though the derivation was based on bubbly flow (Meyer 1981).

5.2.5 Bubble Size

A general form for the bubble radius (assuming bubbles nucleate at an initial radius r_o) from Equation (41) is

$$r^3 = \frac{(n_b)_o}{n_b} r_o^3 + \frac{3\alpha}{n_b 4\pi} \tag{43}$$

where the parameters $(n_b)_o$ and r_o are given constants and n_b is assumed to be a known function of void fraction. The functional variation of bubble radius is proportional to the void fraction and inversely proportional to the bubble density. For empirical comparison or modeling, one of the following simplistic scaling forms from Equation (41) may be more appropriate (for $\alpha > 0$):

$$\begin{aligned}
&1.\quad r = r_r \alpha^{1/3}; && n_b \sim \text{constant} \\
&2.\quad r = r_r; && n_b \sim \alpha \\
&3.\quad r = r_r \left(\frac{\alpha}{1-\alpha}\right)^{1/3}; && n_b \sim 1 - \alpha \\
&4.\quad r = r_r (1-\alpha)^{1/3}; && n_b \sim \frac{\alpha}{1-\alpha}
\end{aligned} \tag{44}$$

where r_r is a measurable reference bubble radii.

Scaling forms 1 and 3 initially underpredict the rate of gas dissolution because the interfacial surface area to liquid volume ratio is very small at low void fractions (i.e., $\alpha \to 0$, $a \to 0$). However, at moderate void fractions ($\alpha > 0.1$), little difference in a is noticeable among the four forms. Consequently, the importance of bubble scaling is in trends produced for various mass transfer coefficients K, bubble radii r, degrees of saturation, system configurations, etc.

5.2.6 Mass Transfer Coefficient

The general correlation for most theoretical studies (Sawa 1975) of mass transfer from bubbles (particles) can be represented by the Sherwood number

$$Sh = f(\pi_r, Sc)$$

where π_r is the bubble Reynolds number and Sc is the Schmidt number. The Sherwood, Schmidt and Reynolds numbers are defined as

$$Sh = \frac{K.d}{\mathcal{D}}$$

$$Sc = \nu_\ell / \mathcal{D} \tag{45}$$

$$\pi_r = \frac{u_\infty d}{\nu_\ell}$$

where d is the bubble diameter, $\mathcal{D}$ is the molecular diffusion coefficient, ν_ℓ is the liquid kinematic viscosity and u_∞ is the relative bubble to liquid velocity.

The mass transfer coefficient correlation used for computational purposes was

$$K = \frac{\mathcal{D}}{d} (2.0 + k\, \pi_r^{1/2}\, Sc^n) \tag{46}$$

where the Schmidt exponent and k coefficient are given by

$n = 1/3$; $k = 0.6$, noncirculating bubbles (spheres) $d < 1$ mm

$n = 1/2$; $k = 0.8$, circulating bubbles $d > 2.5$ mm

The values of the exponent n, coefficient k and transition diameter d were based on the theoretical and experimental work presented by Sawa (1975) and Calderbank and Moo-Young (1961).

Figure 5.1 shows the approximate region of experimentally determined instantaneous mass transfer coefficients versus equivalent spherical diameter by a number of authors, as reported by Meyer (1981). For comparison, the air-water mass transfer coefficient calculated by Equation (46) is included. Based on the above, the mass transfer coefficient in two-phase bubbly flow is expected to range from 1×10^{-4} and 1×10^{-2} m/s.

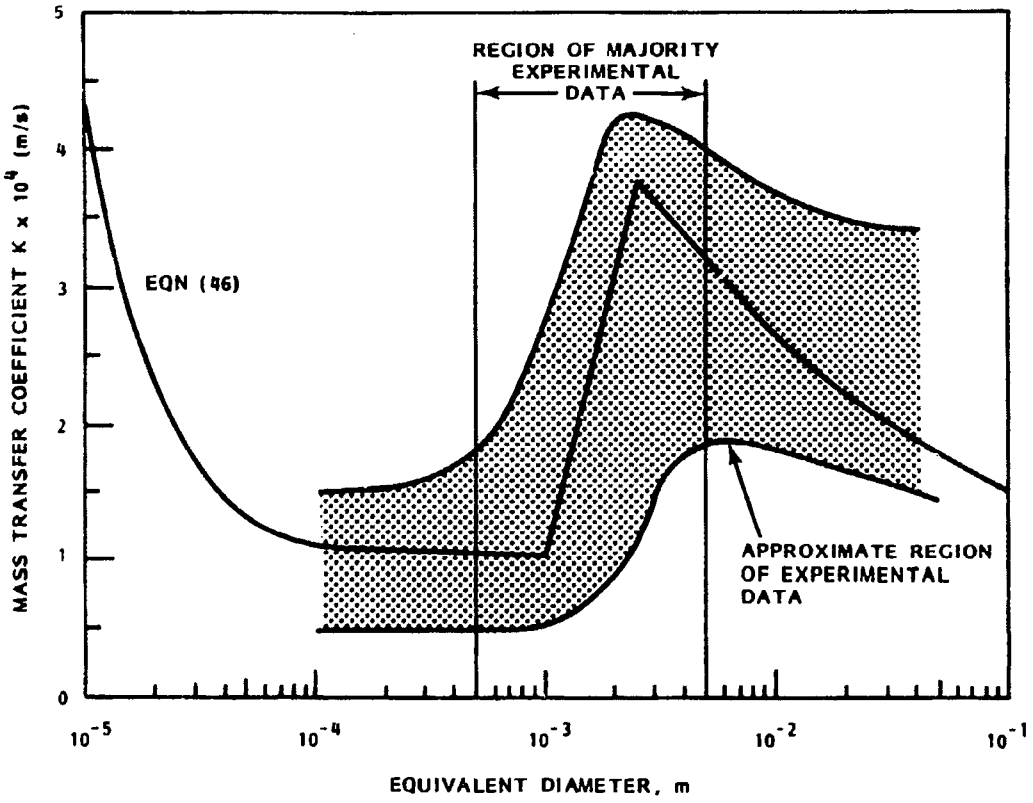

FIGURE 5.1. Mass Transfer Coefficient Versus Equivalent Spherical Diameter, Comparison of Experimental Data and Equation (46) for Air-Water Solutions

5.2.7 Wall Shear Stress

Assuming the multiphase mixture behaves as a Newtonian fluid, the wall shear stress takes the form

$$\tau_w = f\rho_m |u_m| u_m / 8 \tag{47}$$

where f is the Darcy friction factor. The friction factor f reported by Kays (1966) for the smooth tube correlation is

$$f^{-1/2} = -0.8 + 0.87 \ln (\pi_r f^{1/2}) \tag{48}$$

where π_r is the tube Reynolds number based on the two-phase mixture viscosity given by McAdams, Woods, and Heroman (1942).

5.3 STEADY-STATE EQUATIONS OF CHANGE

Steady-state equations of change are developed from the unsteady equations. The major assumptions are the same as those for nonsteady flow. The additional assumptions are:

1. The rate of momentum gain by convective slip is small compared to the mean convective momentum ($\rho_m u_m^2 >> \alpha\rho_v(1-\alpha\rho_v/\rho_m)u_r^2$).
2. The mass flow rate of vapor is small compared to the mass flow rate of liquid plus dissolved gas ($|u_r|/u_\ell << \rho_m/\alpha\rho_v$).
3. The mixture density is approximated by $\rho_m = (1-\alpha)\rho^*$ where $\rho^* \equiv \frac{\alpha\rho_v S}{1-\alpha} + \rho_\ell(1+\Lambda p_c)$ and is a constant. (For homogeneous flow $\rho_m \equiv (1-\alpha)\rho^*$.) This follows from Assumption 2.

The governing steady-state equations were simplified by algebraic substitution to obtain a system of nonlinear initial value differential equations for p and V are (see Meyer 1981)

$$u_\ell = (u_\ell)_o \left(\frac{V+1}{V_o+1}\right)\frac{A_o}{A} \tag{49}$$

$$\frac{dp}{dy} = -\left[A^*\left(\frac{(u_\ell)_o}{V_o+1}\right)^2\left(\frac{D_o}{D}\right)^4 + B^*p\left(1+\frac{V}{S}\frac{\partial s}{\partial V}\right)\right]/C^* \tag{50}$$

$$\frac{dV}{dy} = -\left[A^*/\rho^* + B^*V\right]/C^* \tag{51}$$

where

$$A^* = \left[\Lambda_o\rho_\ell RT/S\left((p_c)_o - \frac{\Lambda}{\Lambda_o}p\right) - Vp + V_o p_o\frac{S_o}{S}\right]\frac{K\,a}{(u_\ell)_o}\frac{A}{A_o}(1+V_o) - \frac{V_p^*}{S}\frac{\partial S}{\partial(D/D_o)}\left(\frac{d(D/D_o)}{dy}\right)$$

$$B^* = \left[g_y + (u_\ell)_o^2\left(\frac{1+V}{1+V_o}\right)^2\left(\frac{D_o}{D}\right)^5\left(\frac{f}{2D_o} - 2\frac{d}{dy}(D/D_o)\right)\right]/(1+V) \tag{52}$$

$$C^* = \frac{p}{\rho^*}\left(1+\frac{V}{S}\frac{\partial S}{\partial V}\right) - \left(\frac{(u_\ell)_o}{1+V_o}\right)^2\left(\frac{D_o}{D}\right)^4 V$$

Slip is defined as

$$S \equiv u_g/u_\ell = 1 + u_r/u_\ell = 1 + \frac{u_t(1 + V_o)}{(u_\ell)_o(1 + V)^{\bar{m}+1}}\left(\frac{D}{D_o}\right)^2 \tag{53}$$

and

$$\frac{\partial S}{\partial V} = \frac{-(\bar{m} + 1)(S - 1)}{1 + V}$$

$$\frac{\partial S}{\partial (D/D_o)} = 2\left[\frac{S - 1}{D/D_o}\right]$$

The above equations are subjected to the boundary conditions

$$y = 0: \quad u_\ell = (u_\ell)_o,\ V = V_o,\ p = p_o,\ p_c = (p_c)_o$$

$$y = \ell: \quad p = p(\ell)$$

where u_ℓ and p at y = 0 must satisfy $p = p(\ell)$ at $y = \ell$.

Identification of C* in Equation (52) with choking for nonhomogeneous flow is presented. The soundspeed for nonhomogeneous two-phase flow without mass transfer is given by

$$C_f^2 \equiv \left(\frac{dp}{d\rho_m}\right)_{p_c=\text{const}} = \frac{P}{\rho^*}\frac{(V + 1)^2}{V}\left[1 + \frac{V}{S}\frac{dS}{dV}\right]$$

and for equilibrium dissolution flow by (54)

$$C_e^2 = \frac{p}{\rho^*}\frac{(V + 1)^2}{V + T/S}\left[1 + \frac{V}{S}\frac{dS}{dV}\right]$$

For a detailed development of these equations see Meyer (1981). Equating liquid velocity in Equations (49) and (53) yields the choking condition

$$\frac{p}{\rho^*}\left[1 + \frac{V}{S}\frac{\partial S}{\partial V}\right] = \left(\frac{(u_\ell)_o}{1 + V_o}\right)^2\left(\frac{D_o}{D}\right)^4 V \tag{55}$$

The similarity between C* and Equation (55) is apparent. The homogeneous choked flow condition is obtained by setting $\partial S/\partial V = 0$. The condition of

choked flow is one in which dp/dy becomes infinite, which from Equation (50) occurs when C* is zero. This choked condition for homogeneous or constant slip flow $\left(\frac{\partial S}{\partial V}\right) = 0$ is similar to that given by Herringe and Davis (1978).

5.4 NONDIMENSIONAL EQUATIONS OF CHANGE

Nondimensionalizing or scaling the equations permits the reduction to a simpler form, thereby reducing (usually) the number of variables. Scaling is also advantageous for numerical compilation and modeling.

5.4.1 Nondimensional Quantities

The dimensionless quantities are:

$$\bar{A} = A/A_o \qquad \pi_h = \rho_\ell g H/p_a$$

$$D^* = D/D_o \qquad \tau_s = \Lambda_o \rho_\ell RT$$

$$P = p/p_a \qquad \pi_1 = gL/u_o^2$$

$$Pa = p_a/\rho_\ell u_o^2 \qquad \pi_f = fL/2D$$

$$P_o = p_o/p_a \qquad \pi_2 = p_a/(\rho_\ell RT)$$

$$(P_c)_o = (p_c)_o/p_a \qquad \tau = u_o t/L$$

$$U_\ell = u_\ell/u_o \qquad \bar{\Lambda} = \Lambda p_a \qquad (56)$$

$$U_m = u_m/u_o \qquad \bar{\Lambda}_c = (\Lambda p_c)$$

$$U_r = u_r/u_o \qquad \lambda = \Lambda/\Lambda_o$$

$$U_o = (u_\ell)_o/u_o \qquad \gamma_1 = a K L/u_o$$

$$Y = y/H \qquad \gamma_2 = \gamma_1/\pi_2$$

$$Z = f(Y) \qquad \gamma_3 = \pi_1 \bar{\rho}_m g_y/g$$

$$f' = dZ/dY \qquad \gamma_4 = \pi_f U_m |U_m| \bar{\rho}_m$$

$$\bar{\rho}_m = \rho_m/\rho_\ell$$

$$\bar{\rho}_g = \rho_g/\rho_\ell$$

$$\bar{\rho}^* = \rho^*/\rho_\ell$$

$$\gamma_5 = \left[\pi_s/S((P_c)_o - \lambda P) - VP + V_o P_o \frac{S_o}{S}\right]\gamma_1 \frac{(D^*)^2}{U_o}(1 + V_o) - \frac{VP}{S}\frac{\partial S}{\partial D^*}\frac{dD^*}{dY}$$

$$\gamma_6 = \left[\frac{g_y L}{u_o^2} + U_o^2\left(\frac{1 + V}{1 + V_o}\right)^2 (D^*)^{-5}\left(\frac{fL}{2D_o} - 2\frac{dD^*}{dY}\right)\right]/(1 + V)$$

$$\gamma_7 = \frac{PaP}{\bar{\rho}^*}\left[1 + \frac{V}{S}\frac{\partial S}{\partial V}\right] - V\left(\frac{U_o}{1 + V_o}\right)^2 D^{*-4}$$

The axial transformation Z = f(Y) is introduced here to provide the option for an unequally spaced mesh in the Y coordinate (equally spaced in Z). This transformation is needed only for unsteady flow analysis and can ensure adequate stacking of nodes in regions of large pressure, velocity and void fraction gradients without requiring that the entire grid be fine meshed.

5.4.2 Nondimensional Unsteady Equations

The governing differential equations [Equations (32) through (35)] with the constitutive relationships take the following forms upon substitution of the nondimensional variables:

Mixture Mass

$$\frac{\partial}{\partial \tau}[\bar{\rho}_m] + \frac{f'(Y)}{\bar{A}}\frac{\partial}{\partial \bar{Z}}[\bar{\rho}_m U_m \bar{A}] = 0 \tag{57}$$

Vapor Mass

$$\frac{\partial}{\partial \tau}[\alpha P] + \frac{f'(Y)}{\bar{A}}\frac{\partial}{\partial \bar{Z}}[\alpha P U_m \bar{A}] + \frac{f'(Y)}{\bar{A}}\frac{\partial}{\partial \bar{Z}}\left[\alpha P\left(1 - \frac{\alpha P \pi_2}{\bar{\rho}_m}\right)U_r \bar{A}\right] = \gamma_2(\bar{\Lambda}_c - \bar{\Lambda} P) \tag{58}$$

Total Gas Mass

$$\frac{\partial}{\partial \tau}[\bar{\rho}_g] + \frac{f'(Y)}{\bar{A}}\frac{\partial}{\partial \bar{Z}}[\bar{\rho}_g U_m \bar{A}] + \frac{f'(Y)}{\bar{A}}\frac{\partial}{\partial \bar{Z}}\left[\alpha P \pi_2\left(1 - \frac{\bar{\rho}_g}{\bar{\rho}_m}\right)U_r \bar{A}\right] = 0 \tag{59}$$

Momentum

$$\frac{\partial}{\partial \tau}[\bar{\rho}_m U_m] + \frac{f'(Y)}{\bar{A}}\frac{\partial}{\partial \bar{Z}}\left[\bar{\rho}_m U_m^2 \bar{A}\right] + \frac{f'(Y)}{\bar{A}}\frac{\partial}{\partial \bar{Z}}\left[\alpha P \pi_2\left(1 - \frac{\alpha P \pi_2}{\bar{\rho}_m}\right)U_r^2 \bar{A}\right]$$

$$= - Paf'(Y)\frac{\partial P}{\partial \bar{Z}} - \gamma_3 - \gamma_4. \tag{60}$$

Equations (57) through (60) represent the equations required for numerical computation along with the boundary conditions

$Y = 0$: INFLOW; $P = P_o$, $\alpha = \alpha_o$, $\bar{\rho}_m = (\bar{\rho}_m)_o$, $\bar{\rho}_g = (\bar{\rho}_g)_o$

OUTFLOW; $P = P_o$

$Y = 1$: OUTFLOW; $P = P(\tau, Y = 1)$

INFLOW; $P = P(\tau, Y = 1)$, $\alpha = \alpha(\tau, Y = 1)$, $\bar{\rho}_m = \bar{\rho}_m(\tau, Y = 1)$, $\bar{\rho}_g = \bar{\rho}_g(\tau, Y = 1)$

5.4.3 Nondimensional Steady-State Equations

The governing steady-state Equations (49), (50) and (51) for U_ℓ, P and V take on the following forms upon substitution of the dimensionless variables:

$$U_\ell = U_o \left(\frac{V + 1}{V_o + 1}\right)(D^*)^{-2} \tag{61}$$

$$\frac{dP}{dY} = F(Y,P,V) \tag{62}$$

$$\frac{dV}{dY} = G(Y,P,V) \tag{63}$$

where

$$F(Y,P,V) = -\left[\left(\frac{U_o}{V_o + 1}\right)^2 \frac{\gamma_5}{(D^*)^4} + P\left(1 + \frac{V}{S}\frac{\partial S}{\partial V}\right)\gamma_6\right] / \gamma_7 \tag{64}$$

$$G(Y,P,V) = \left[\frac{Pa}{\bar{\rho}^*}\gamma_5 + V\gamma_6\right] / \gamma_7$$

The above equations are subject to the boundary conditions

$$Y = 0: \quad U_\ell = U_o, \; V = V_o$$

$$Y = 1: \quad P = 1$$

where U_ℓ and P at $Y = 0$ must satisfy $P = 1$ at $Y = 1$.

The inlet saturation pressure $(P_c)_o$ and the inlet system pressure P_o at Y = 0 can be represented respectively by

$$(P_c)_o = \pi_h \eta_1 + 1$$

and (65)

$$P_o = \pi_h \eta_2 + 1 - C_L U_o^2/2Pa$$

where η_1 is the degree of saturation, η_2 is the degree of pressurization, $U^2/2Pa$ is the inlet velocity head and C_L is the inlet loss coefficient. For $\eta_1 = 1$ and $\eta_2 = 1$ the inlet concentration and cavern pressures are equal to the liquid hydrostatic head.

5.5 NUMERICAL FORMULATION

The differential equations are first approximated by a finite-difference scheme. The steady-state difference equations are solved by a predictor-corrector method with shooting. The unsteady equations are solved by a modified parallel method. The theoretical objectives are to determine pressure, void fraction and velocity axial profiles for various mass transfer parameters, system configurations and design transients. The numerical formulation details are provided by Meyer (1981).

5.5.1 Steady-State Numerical Formulation

Equations (61) and (62) constitute a system of nonlinear initial-value differential equations for P and V. These equations are solved numerically by a variable step-size predictor-corrector method with local error control. Approximations to P and V will be generated at various mesh points in the Y internal (0,1) where P_i and V_i approximate the exact solutions $P(Y_i)$ and $V(Y_i)$.

The procedure uses the implicit Adams-Moulton three-step method to improve upon approximations obtained by the explicit Adams-Bashforth four-step method. This combination of an explicit and implicit technique (predictor-corrector method) is similar to that reported by Burden, Faires and Reynolds (1978) for initial value problems. Provided the difference

between the initial (explicit method) and final (implicit method) approximations are within a specified tolerance, the final values of P_{i+1} and V_{i+1} would then be used as approximations to $P(Y_{i+1})$ and $V(Y_{i+1})$. The technique of using the Adams-Bashforth as a predictor and the Adams-Moulton method as the corrector is then repeated for the next mesh point. Because the multistep methods require equal step sizes for the starting values, any change in step size necessitates recalculating new starting values at that point. This is done by calling a Runge-Kutta subroutine. The exit values for P and V at the last mesh point N ($Y_N = 1$) are also calculated via the Runge-Kutta method where $\Delta Y_N = 1 - Y_{N-1}$.

This scheme of solving the system of differential equations is combined with an iterative procedure on the inlet velocity U_o at Y = 0 to achieve the exit pressure $P_N = 1$ at $Y_N = 1$. The iterative procedure on the inlet velocity U_o involves a secant method to find the root of the equation $(P_N - 1) = 0$. This is similar to a shooting method. The numerical procedure is continued until $(P_N - 1) < \varepsilon$ where ε is a specified tolerance.

The procedure is complete with the values of liquid and vapor velocities calculated from Equations (61) and (53), respectively:

Liquid

$$(U_\ell)_i = U_o \frac{V_i + 1}{V_o + 1} (D_i^*)^{-2}$$

Vapor

$$(U_g)_i = S_i (U_\ell)_i .$$

5.5.2 Unsteady Numerical Formulation

A revised method of calculating one-dimensional transient multiphase flow is presented, based on modifications of the implicit multifield (IMF) method and implicit continuous-fluid Eulerian (ICE) technique.

This method incorporates the flexibility for variable advanced-timing of convective terms ranging from a fully implicit to a purely explicit

form. The method also incorporates spatial coupling of pressure and incremental pressure terms (Stewart 1979), resulting in order-of-magnitude gains in computation time. The numerical finite difference method is useful for all Mach numbers from zero (incompressible limit) to infinity.

The papers of Harlow and Amsden (1971, 1975), Stewart (1979), Liles and Reed (1978) and Ramshaw and Trapp (1976) are recommended as general references to the current state-of-the-art numerical techniques for calculating transient two-phase flow.

5.6 DIFFERENCE EQUATIONS

A fragment of the Eulerian finite-difference mesh illustrating the centering of field variables relative to a typical cell is depicted in Figure 5.2. The mass equations are differenced over the mesh cells indicated by dashed lines; the momentum equation is differenced over the solid cells. The index i counts cell centers (solid lines) from left to right while the cell edges (dashed lines) are labeled with an index $i \pm 1/2$.

The finite differenced equations for the continuity and momentum equations from Equations (57) through (60) are:

Mixture Mass

$$\frac{(\bar{\rho}_m)_i^{n+1} - (\bar{\rho}_m)_i^n}{\delta\tau} + \frac{f'_i\theta}{\bar{A}_i\delta Z}\left[\bar{A}_{i+1/2}\,(\bar{\rho}_m U_m)_{i+1/2}^{n+1} - \bar{A}_{i-1/2}\,(\bar{\rho}_m U_m)_{i-1/2}^{n+1}\right] \qquad (66)$$

$$+ \frac{f'_i}{\bar{A}_i}\,\frac{1-\theta}{\delta Z}\left[\bar{A}_{i+1/2}\,(\bar{\rho}_m U_m)_{i+1/2}^{n} - \bar{A}_{i-1/2}\,(\bar{\rho}_m U_m)_{i-1/2}^{n}\right] = 0$$

Vapor Mass

$$\frac{\alpha_i^{n+1} P_i^{n+1} - \alpha_i^n P_i^n}{\delta\tau} + \frac{f'_i\theta}{\bar{A}_i\delta Z}\left[\bar{A}_{i+1/2}(\alpha P U_m)_{i+1/2}^{n+1} - \bar{A}_{i-1/2}(\alpha P U_m)_{i-1/2}^{n+1}\right] \qquad (67)$$

$$= RV_i^n + (1-\theta)S_i^n + \theta S_i^{n+1}$$

COMPUTATIONAL CELLS

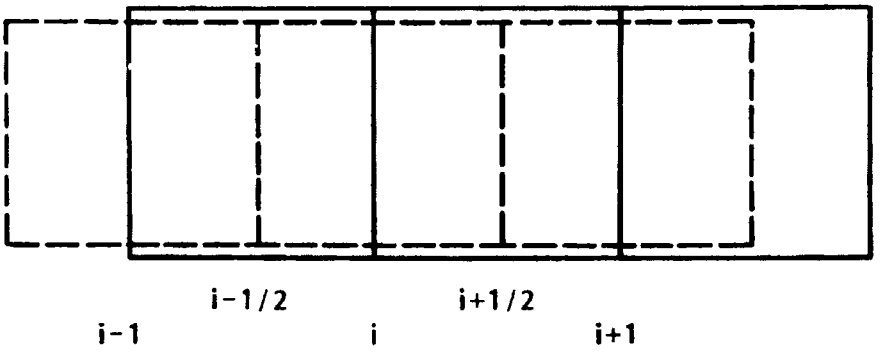

MOMENTUM CELL

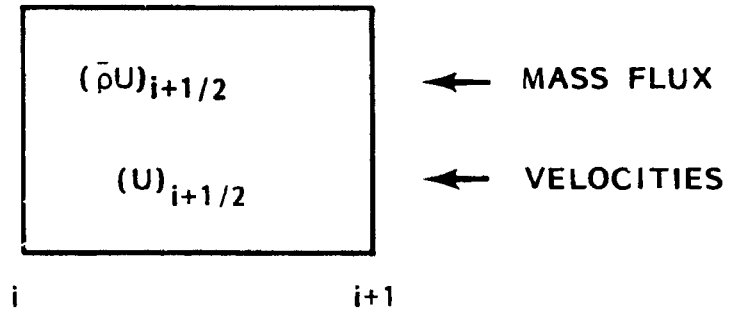

CONTINUITY CELL

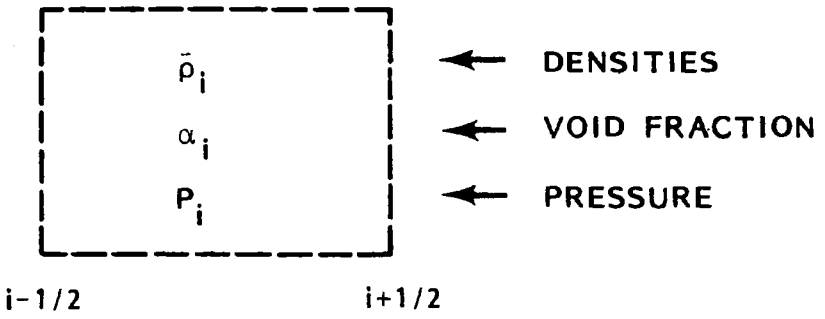

FIGURE 5.2. Eulerian Finite Difference Mesh Labeling Convention

Total Gas Mass

$$\frac{(\bar{\rho}_g)_i^{n+1} - (\bar{\rho}_g)_i^n}{\delta\tau} + \frac{f'_i\theta}{\bar{A}_i\delta Z}\left[\bar{A}_{i+1/2}(\bar{\rho}_g U_m)_{i+1/2}^{n+1} - \bar{A}_{i-1/2}(\bar{\rho}_g U_m)_{i-1/2}^{n+1}\right] = RG_i^n \tag{68}$$

Momentum

$$\frac{(\bar{\rho}_m U_m)_{i+1/2}^{n+1} - (\bar{\rho}_m U_m)_{i+1/2}^{n}}{\delta\tau} = \frac{Paf'_{i+1/2}}{\delta Z}\left[\phi\left(P_i^{n+1} - P_{i+1}^{n+1}\right)\right. \tag{69}$$

$$\left. - (1-\phi)\left(P_i^n - P_{i+1}^n\right)\right] + R_{i+1/2}^n$$

The terms in the above equations that contain no advanced-time factors are defined as:

$$R_{i+1/2}^n = -\frac{f'_{i+1/2}}{\bar{A}_{i+1/2}\delta Z}\left[A_{i+1}\alpha_{i+1}^n P_{i+1}^n \pi_2\left(1 - \frac{\alpha_{i+1}^n P_{i+1}^n \pi_2}{(\bar{\rho}_m)_{i+1}}\right)(U_r)_{i+1}^2\right.$$

$$\left. - \bar{A}_i\alpha_i^n P_i^n \pi_2\left(1 - \frac{\alpha_i^n P_i^n \pi_2}{(\bar{\rho}_m)_i}\right)(U_r)_i^2\right]$$

$$- \frac{f'_{i+1/2}}{\bar{A}_{i+1/2}\delta Z}\left[\bar{A}_{i+1}(\bar{\rho}_m U_m^2)_{i+1}^n - \bar{A}_i(\bar{\rho}_m U_m^2)_i^n\right] - (\gamma_3)_{i+1/2}^n - (\gamma_4)_{i+1/2}^n \tag{70}$$

$$RG_i^n = -\frac{f'_i(1-\theta)}{\bar{A}_i\delta Z}\left[\bar{A}_{i+1/2}(\bar{\rho}_g U_m)_{i+1/2}^n - \bar{A}_{i-1/2}(\bar{\rho}_g U_m)_{i-1/2}^n\right]$$

$$- \frac{f'_i\pi_2}{\bar{A}_i\delta Z}\left[\bar{A}_{i+1/2}\left(\alpha P\left(1 - \frac{\bar{\rho}_g}{\bar{\rho}_m}\right)U_r\right)_{i+1/2}^n\right.$$

$$\left. - \bar{A}_{i-1/2}\left(\alpha P\left(1 - \frac{\bar{\rho}_g}{\bar{\rho}_m}\right)U_r\right)_{i-1/2}^n\right]$$

$$RV_i^n = \frac{f_i'(1-\theta)}{\bar{A}_i \delta Z}\left[\bar{A}_{i+1/2}(\alpha P U_m)^n_{i+1/2} - \bar{A}_{i-1/2}(\alpha P U_m)^n_{i-1/2}\right]$$

$$- \frac{f_i'}{\bar{A}_i \delta Z}\left[\bar{A}_{i+1/2}\left(\alpha P\left(1 - \frac{\alpha P \pi_2}{\bar{\rho}_m}\right)U_r\right)^n_{i+1/2}\right.$$

$$\left. - \bar{A}_{i-1/2}\left(\alpha P\left(1 - \frac{\alpha P \pi_2}{\bar{\rho}_m}\right)U_r\right)^n_{i-1/2}\right]$$

$$S_i^n = (\gamma_2)_i^n\left[(\bar{\Lambda}_c)_i^n - \bar{\Lambda}_i^n P_i^n\right].$$

The finite difference forms for the total gas density and mixture density are:

$$(\bar{\rho}_g)_i^{n+1} = \left(1 - \alpha_i^{n+1}\right)(\bar{\Lambda}_c)_i^{n+1} + \alpha_i^{n+1} P_i^{n+1} \pi_2 \tag{71}$$

and

$$(\bar{\rho}_m)_i^{n+1} = (\bar{\rho}_g)_i^{n+1} + 1 - \alpha_i^{n+1} \tag{72}$$

The index n + 1 indicates an advanced-time value while the old time value is denoted by n. The weighting constants θ and ϕ, with magnitudes between 0 and 1, denote the relative level of time centering of the mixture mass and pressure terms, respectively. For $\theta = \phi = 1$, that term is evaluated at the advanced time (implicitly), whereas, for $\theta = \phi = 0$, the method is explicit.

The numerical iterative procedure for the pressure increments requires the mixture continuity and momentum equation to be represented in slightly different notational forms. The revised form enables identification of before and after iteration increments.

The following variables are now defined:

$$\begin{aligned} P_i^{n+1} &\equiv \hat{P}_i + \delta P_i \\ (\bar{\rho}_m)_i^{n+1} &\equiv (\tilde{\bar{\rho}}_m)_i + \delta\bar{\rho}_i \\ (\bar{\rho}_m U_m)^{n+1}_{i+1/2} &\equiv (\tilde{\bar{\rho}}_m \tilde{U}_m)_{i+1/2} + \delta(\bar{\rho}_m U_m)_{i+1/2} \\ \Delta\bar{\rho}_i &= (\tilde{\bar{\rho}}_m)_i - (\hat{\bar{\rho}}_m)_i \end{aligned} \tag{73}$$

where the δ operator represents small increments in the given variable.

The other needed relationships are the equation of state pressure functions

$$P_i^{n+1} = P_i^n + 1/C_i^n \left[(\bar{\rho}_m)_i^{n+1} - (\bar{\rho}_m)_i^n\right] \tag{74}$$

and

$$\delta P_i = 1/C_i^n \delta\bar{\rho}_i \tag{75}$$

where $C_i^n \equiv \left(\frac{d\bar{\rho}_m}{dP}\right)_i^n$ is the inverse of the nondimensional sound speed squared.

The use of Equation (74) is extremely advantageous for cases involving single-phase vapor flow or those involving large spatial variations in void fractions where the density differences are related to pressure phenomena and not convection. Equation (75) is required for pressure incrementation.

The convective mixture mass flux from the mixture momentum Equation (69) can now be represented by

$$(\bar{\rho}_m\tilde{U}_m)_{i+1/2} = (\bar{\rho}_m U_m)_{i+1/2}^n + Paf'_{i+1/2} \frac{\delta\tau}{\delta Z} \left[\phi(\hat{P}_i - \hat{P}_{i+1}) - (1-\phi)(P_i^n - P_{i+1}^n)\right] + R_{i+1/2}^n \tag{76}$$

and

$$\delta(\bar{\rho}_m U_m)_{i+1/2} = Paf'_{i+1/2} \frac{\delta\tau}{\delta Z} \phi[\delta P_i - \delta P_{i+1}] \tag{77}$$

The mixture continuity Equation (66) by substitution of Equation (73) becomes

$$\delta\bar{\rho}_i + \frac{f'_i\theta}{\bar{A}_i \delta Z}\left[\bar{A}_{i+1/2}\delta(\bar{\rho}_m U_m)_{i+1/2} - \bar{A}_{i-1/2}\delta(\bar{\rho}_m U_m)_{i-1/2}\right] = -(\tilde{\bar{\rho}}_m - \hat{\bar{\rho}}_m)_i \tag{78}$$

where

$$(\hat{\bar{\rho}}_m)_i \equiv (\bar{\rho}_m)_i^n + \frac{f_i' \theta \delta\tau}{\bar{A}_i \delta Z} \left[\bar{A}_{i-1/2} (\bar{\rho}_m \tilde{U}_m)_{i-1/2} - \bar{A}_{i+1/2} (\bar{\rho}_m \tilde{U}_m)_{i+1/2} \right] \tag{79}$$

$$+ \frac{f_i' (1 - \theta) \delta r}{\bar{A}_i \delta Z} \left[\bar{A}_{i-1/2} (\bar{\rho}_m U_m)_{i-1/2}^n - \bar{A}_{i+1/2} (\bar{\rho}_m U_m)_{i+1/2}^n \right]$$

Elimination of $\delta (\bar{\rho}_m U_m)_{i+1/2}$ and $\delta \bar{\rho}_i$ from Equation (78) by algebraic substitution of Equations (75) and (77) results in the implicit pressure increment equation

$$-C_i^n \delta P_i + \frac{\theta \phi f_i' Pa}{\bar{A}_i} \left(\frac{\delta\tau}{\delta Z} \right)^2 \left[f'_{i-1/2} \bar{A}_{i-1/2} \delta P_{i-1} - (f'_{i-1/2} \bar{A}_{i-1/2} + f'_{i+1/2} \bar{A}_{i+1/2}) \delta P_i \right.$$

$$\left. + f'_{i+1/2} \bar{A}_{i+1/2} \delta P_{i+1} \right] = \Delta \bar{\rho}_i \tag{80}$$

5.7 SOLUTION PROCEDURE

The numerical method to solve the governing finite-difference equations is a combination of the implicit multifield (IMF) methods of Stewart (1979) and Harlow and Amsden (1975) and the implicit continuous-fluid Eulerian (ICE) technique of Harlow and Amsden (1971). The essential features of this method enable implicit treatment of the continuity equations and the pressure field. As in the IMF technique, the new pressures are determined by iteration.

The solution procedure requires an iterative procedure, for which the following notation is introduced: values at the beginning of each iteration will be indicated by a circumflex (^), values resulting from the iteration will be denoted by a tilda (~).

The solution procedure is outlined as follows:

Step 1. Calculate the required beginning-of-cycle terms $R_{i+1/2}$, $RG_{i+1/2}^n$, $RV_{i+1/2}^n$, S_i^n, G_i^n, and C_i^n. These terms contain no advanced-time factors and remain constant during the iterative portion of the solution procedure.

Step 2. Initiation of the beginning-of-cycle pressure profile $\hat{P}_i$. This can be accomplished in a number of ways, depending on the particular two-phase flow problem dictating the degree of coupling of neighboring pressure terms (Meyer 1981).

Step 3. Solve for the momentum flux $(\bar{\rho}\tilde{U}_m)_{i+1/2}$, from the estimated pressure profile $\hat{P}_i$ using Equation (76).

Step 4. Calculate the beginning-of-cycle density $(\hat{\bar{\rho}}_m)_i$ from Equation (79).

Step 5. Solve for the mixed mean velocity.

$$(\tilde{U}_m)_{i+1/2} = (\bar{\rho}_m\tilde{U}_m)_{i+1/2}/(\hat{\bar{\rho}}_m)_{i+1/2}$$

where $(\hat{\bar{\rho}}_m)_{i+1/2}$ is calculated by a predetermined "weight donor cell" method.

Step 6. From the new velocities $(\tilde{U}_m)_{i+1/2}$ and pressure $\hat{P}_i$ the total gas density is calculated from Equation (68). The pressure concentration $(\tilde{\Lambda}_c)_i$ and void fraction $\bar{\alpha}_i$ are then calculated by an iterative procedure using Equation (71).

Step 7. Calculate the updated mixed mean density from Equation (72):

$$(\tilde{\bar{\rho}}_m)_i = (\tilde{\bar{\rho}}_g)_i + 1 - \tilde{\alpha}_i$$

Step 8. Calculate the difference between $(\tilde{\bar{\rho}}_m)_i$ and $(\hat{\bar{\rho}}_m)_i$, finding the differences not zero but equal to some remainder $\Delta\bar{\rho}_i$,

$$\Delta\bar{\rho}_i = (\tilde{\bar{\rho}}_m)_i - (\hat{\bar{\rho}}_m)$$

Step 9. The remainders in Step 8 are then used to determine increments δP_i for the estimated pressures, so that $\tilde{P}_i = \hat{P}_i + \delta P_i$. If the increments in $\Delta\bar{\rho}_i$ and δP_i are not smaller than specified errors, the new pressure profile $(\tilde{P}_i)$ is used to recommence the iteration. The pressure increments are calculated from Equation (80):

$$C_i^n\delta P_i + \theta\phi\frac{f_i'Pa}{\bar{A}_i}\left(\frac{\delta\tau}{\delta Z}\right)^2\left[-f'_{i-1/2}\bar{A}_{i-1/2}\delta P_{i-1} + (f'_{i-1/2}\bar{A}_{i-1/2} + f'_{i+1/2}\bar{A}_{i+1/2})\delta P_i\right.$$

$$\left.-f'_{i+1/2}\bar{A}_{i+1/2}\delta P_{i+1}\right] = -\omega^*\Delta\bar{\rho}_i$$

where ω^* is an over-/under-relaxation parameter whose slight variations above or below unity accomplish over- or under-relaxation. This system of equations can be represented by the tridiagonal matrix and solved by Gaussian elimination for δP_i.

Step 10. The tilda values of pressure and density are now updated by

$$\tilde{P}_i = P_i + \delta P_i$$

and

$$(\tilde{\bar{\rho}}_m)_i = (\hat{\bar{\rho}}_m)_i + C_i^n \delta P_i$$

If the incremental pressures δP_i or densities $\Delta\bar{\rho}_i$ are not within specified tolerances, the circumflex values are updated by setting them equal to the tilda values. The circumflex values of the mass flux are updated as in Step 3 and the procedure is recommenced starting at Step 5. Because the error reduction is about an order of magnitude per iteration, rarely are more than a few iterations necessary.

If the increments in pressure and mixed mean density are smaller than prescribed tolerances, the field variables at time n + 1 are approximated by the tilda values and the process recommences with Step 1.

5.8 SCALING HYPOTHESIS COMPARISON

The scaling hypothesis assumes a fundamental form for the bubble radius exists. A few simplistic scaling forms are given by Equation (44).

The purpose of the hypothesis is to reduce Equations (62) and (63) into forms that are more elementary and less dependent on the interfacial area parameters at the onset of nucleation. One way to achieve this simplification is to assume a bubble radius relationship of the form

$$r = r_r V^{1/3} \tag{81}$$

where r_r is a measurable reference bubble radii and V is the gas-liquid volume fraction. A simplistic form for the interfacial area from Equation (42) is

$$a = \frac{3\alpha}{r} \tag{82}$$

where the initial bubble radii and interfacial area were assumed to be zero in accordance with Equation (81). Substituting Equation (81) into (82) results in the following gas-liquid interfacial area

$$a = \frac{3V^{2/3}}{r_r(1 + V)} \tag{83}$$

which is a function of V. The only input parameters required to obtain the interfacial area is the measurable reference bubble radius r_r.

Equation (63) is not in a convenient form to take advantage of this simplistic approach of modeling the interfacial area, because the rate of change of V with respect to Y will be zero (dV/dY = 0) for all flows that begin as single-phase liquids. That is, γ_5 [see Equation (56)] will be zero unless an initial gas-liquid interfacial area exists at V = 0 to initiate dissolution. To avoid this problem, Equations (56) and (61) through (64) can be written in terms of $\bar{V}$ which is the cube root of V ($\bar{V} \equiv V^{1/3}$). This substitution ensures the spatial gradient of $\bar{V}$ is not equal to zero at zero gas-liquid fractions $d\bar{V}/dY \neq 0$ at $\bar{V} = 0$. An equivalent but more convenient form of these equations for this application is obtained by rewriting the equations in terms of $\bar{V}$. The resulting initial value differential equations for P and $\bar{V}$ are

$$\frac{dP}{dY} = -\left[\left(\frac{U_o}{\bar{V}^3 + 1}\right)^2 \frac{\gamma_5^* \bar{V}^2}{(D^*)^4} + P\left(1 + \frac{\bar{V}}{3S}\frac{\partial S}{\partial \bar{V}}\right)\gamma_6\right]/\gamma_7 \tag{84}$$

$$\frac{d\bar{V}}{dY} = \left[\frac{Pa}{\bar{\rho}^*}\gamma_5^* + \bar{V}\gamma_6\right]/(3\gamma_7) \tag{85}$$

where

$$\gamma_1^* = \gamma_1/V^{2/3} = \frac{KL}{u_o r_r(1 + \bar{V}^3}$$

$$\gamma_5^* = \left[\pi_s/S\left((P_c)_o - \lambda P\right) - \bar{V}^3 P + \bar{V}_o^3 P_o \frac{S_o}{S}\right]\gamma_1^* \frac{A'}{A_o}(1 + \bar{V}_o^3) \tag{86}$$

$$- \frac{\bar{V}P}{S}\frac{\partial S}{\partial D^*}\frac{dD^*}{dY}$$

For a supersaturated solution with no initial gas-liquid interfacial surface area dV/dY is greater than zero causing gas dissolution. The scaling hypothesis initial dissolution process thus assumed gas bubbles nucleate at zero radius.

Solution of the above system of nonlinear initial value problems results in pressure, void fraction and velocity profiles similar to the more complex model profiles. Figure 5.3 illustrates the effect of the mass transfer coefficient (K/r_r ratios) on void fraction profiles for the scaling hypothesis. Figure 5.3 clearly shows the same general trends and characteristics as the more complicated model. The scaling hypothesis also is shown to asymptote to the full dissolution void fraction value for large K/r_r values.

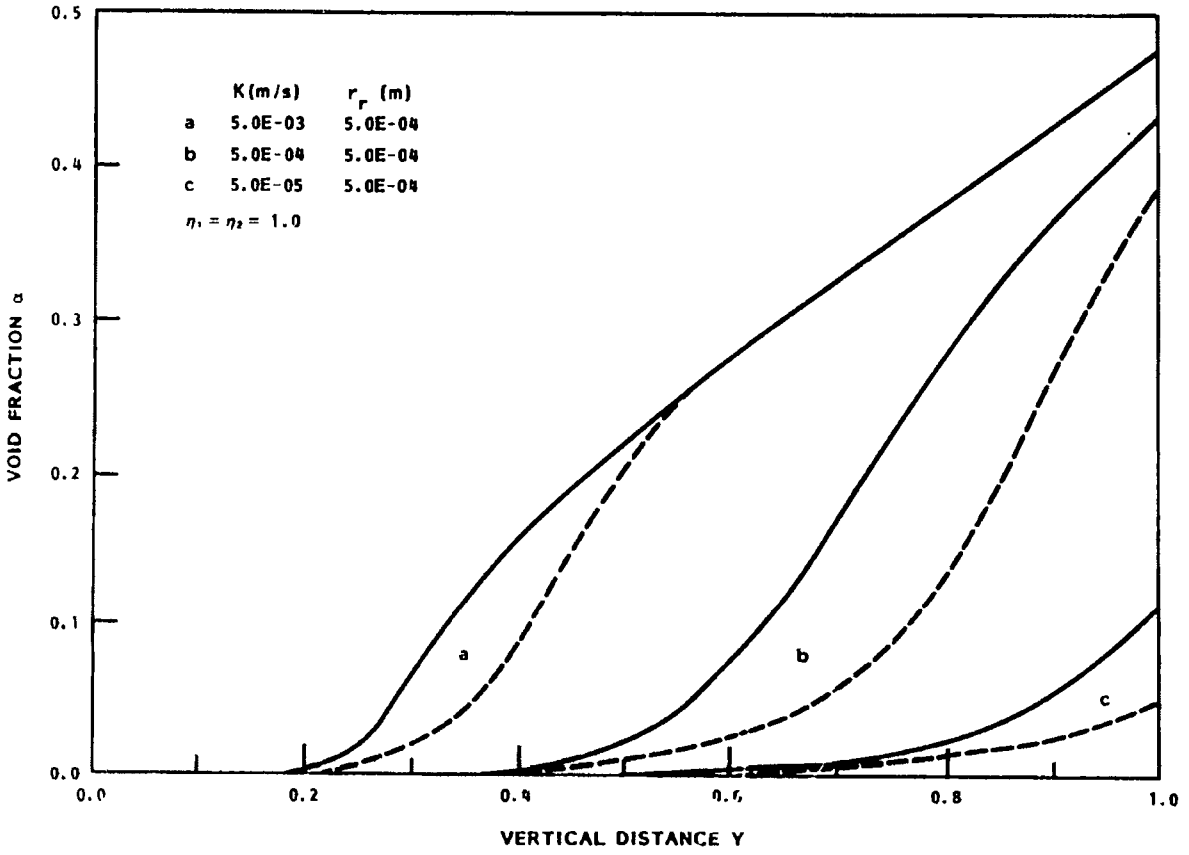

FIGURE 5.3. Comparison of Comprehensive and Scaling Hypothesis Void Fraction Profiles for Various Mass Transfer Coefficients (RPI Model)

The scaling model void fraction and velocity profiles are very close to the corresponding profiles with nucleation densities of order 10^7 bubbles/m^3. Since nucleation density must be changed by an order of magnitude to make any appreciable effect on the profiles, the scaling hypothesis should be in reasonable agreement for systems with nucleation densities of the order $10^7/m^3$. The similarity between these interfacial area models is not all that surprising because both have nearly the same interfacial areas at relatively small void fractions (i.e., for $\alpha > 4/3\pi(n_b)_o^3 r_o$; $a \rightarrow 3\alpha/r$).

The scaling hypothesis model provides the user with a simplistic model for determining the effects of various parameters without knowledge of the actual nucleation process or nucleation density. The only required input is a measurable equivalent reference bubble radius.

5.0 BLOWOUT PHENOMENON

A blowout is a potential problem during CAES system charging. If the influx of gas during charging is sufficient to displace the liquid in the lower reservoir to the bottom of the U-bend, compressed gas could escape through the compensation shaft and cause a system blowout. Termination of the charging process may not prevent blowout, however, once the lower reservoir has reached a low liquid level. Blowout would occur, for instance, if conditions existed such that the buoyancy-driven two-phase efflux from the reservoir lowered the liquid level in the U-bend to a point where the two-phase hydrostatic density head was insufficient to maintain a liquid level in the bend. A U-bend is incorporated to prevent this from occurring; its depth can be predetermined from the operational lower reservoir pressure and buoyancy-dissolution effects.

The U-bend depth must be designed so that if liquid is displaced to the bottom of the U-bend, the lower reservoir pressure will be insufficient to overcome the viscous, gravitational and two-phase acceleration forces acting in the compensation shaft. This would cause a reverse flow, which would force liquid back into the lower reservoir and prevent blowout.

Based on Meyer (1981), the maximum U-bend depth to height ratio to prevent blowout for given degrees of saturation and pressurization are

$\underline{\eta_1 > \eta_2}$

$$\frac{h_b}{H} = \frac{1}{\bar{\rho}_*}\left[\eta_2(1 - \pi_s) + \pi_s\left(\eta_1 + \frac{1}{\pi_h}\right)\ell n\ (\pi_h\eta_2 + 1)\right] - 1 \qquad (87)$$

$\underline{\eta_2 > \eta_1}$

$$\frac{h_b}{H} = \frac{1}{\bar{\rho}^*}\left[\eta_2 - \pi_s\eta_1 + \pi_s\left(\eta_1 + \frac{1}{\pi_h}\right)\ell n(\pi_h\eta_1 + 1)\right] - 1$$

where the nondimensional variables [Equation (56)] and nondimensional saturation and tank pressures [Equation (65)] have been incorporated. The blowout phenomenon will not occur for U-bend depth to height ratios greater than those given in Equation (87).

A number of U-bend depth to height ratios for the RPI high solubility (carbon dioxide/water) and the Potomac Electric Power Company (PEPCO) CAES prototype (air/water) systems appear in Table 5.1. The results are shown for various degrees of saturation and pressurization. Typical U-bend depth to height ratios to prevent blowout for the PEPCO prototype and RPI model are 0.065 and 0.349, respectively, for $\eta_1 = \eta_2 = 1$.

5.10 COMPRESSED AIR ENERGY STORAGE DESIGN TRANSIENT

The unsteady model was used to investigate the dynamic response of the proposed PEPCO CAES system for a typical charging transient. The design charging cycle transient and system parameters were obtained from a design report prepared by Willett and Shippey (1980). A schematic of the system, pertinent dimensions and air-water properties are given by Meyer (1981).

Initially, the system is in static equilibrium at the lower reservoir mid-water level. The water in the compensation shaft is assumed to be saturated at the local hydrostatic pressure, as is the lower reservoir

TABLE 5.1. U-Bend Depth to Height Ratios to Prevent Blowout for the PEPCO Prototype and RPI Model

	Prototype (H = 735 m) (π_h = 71.088, π_s = 0.02015)		RPI Model (H = 10 m) (π_h = 0.96718, π_s = 0.9408)	
η_1	η_2	h_b/H	η_2	h_b/H
0.50	0.9746	0	0.9045	0
0.50	1.0	0.0254	1.0	0.0952
0.50	1.1	0.1254	1.1	0.1948
0.50	1.2	0.2251	1.2	0.2945
0.50	1.3	0.3249	1.3	0.3942
0.50	1.5	0.5245	1.5	0.5935
0.75	0.9603	0	0.7935	0
0.75	0.98	0.0196	0.9	0.1061
0.75	1.0	0.0396	1.0	0.2058
0.75	1.1	0.1394	1.1	0.3054
0.75	1.2	0.2393	1.2	0.4051
0.75	1.5	0.5387	1.5	0.7041
1.0	0.9345	0	0.6765	0
1.0	0.95	0.0155	0.85	0.1944
1.0	1.0	0.0654	1.0	0.3493
1.0	1.1	0.1652	1.1	0.4490
1.0	1.2	0.2650	1.2	0.5487
1.0	1.5	0.5645	1.5	0.8476
1.25	0.9125	0	0.5886	0
1.25	0.95	0.0367	0.7	0.1437
1.25	1.0	0.0869	0.8	0.2745
1.25	1.1	0.1871	1.0	0.5079
1.25	1.2	0.2871	1.2	0.7206
1.25	1.5	0.5866	1.5	1.0201

water. This system's saturation level is assumed to be a worst case condition. The charging transient is initiated with the start of the compressors, which force compressed air into the lower reservoir at a rate of 1200 kg/s. The charging rate is constant and continues for 1000 s, at which time the compressors are turned off.

Because of the large amount of compressible gas in the lower reservoir, the above transient creates an oscillating behavior similar to a spring-mass system. The period of oscillation T* for this system containing a single-phase fluid can be shown to be approximately

$$T^* = \frac{2\pi}{\sqrt{\frac{(P_t)_o A}{(V_g^*)_o \rho_\ell L}}} \tag{88}$$

where

$(P_t)_o$ = initial lower reservoir gas pressure N/m^2

$(V_g^*)_o$ = initial lower reservoir gas volume m^3

L = total shaft length m

A = shaft area m^2

ρ_ℓ = liquid density kg/m^3

Equation (88) is the same as that proposed by Larsen and Norén (1973) for a simplified single-phase model to predict the oscillatory dynamic response of a CAES system.

This oscillatory behavior also results in a phase shift angle of $\pi/2$ radians between the pressure and velocity amplitudes. For a detailed derivation of Equation (88) and phase angle, the reader is referred to Meyer (1981).

Equation (88) demonstrates that, if the compensation shaft length or gas volume in the lower reservoir increases, the period of oscillation will also increase. Conversely, if the tank pressure or shaft area were increased, the period of oscillation would decrease. These general trends have been shown by McMonagle and Rowe (1980).

From Equation (88), the period of oscillation for the present PEPCO design transient with input values

$$(P_t)_o = 7.3 \times 10^6 \text{ N/m}^2$$

$$(V_g^*)_o = 3.0 \times 10^5 \text{ m}^3$$

$$L = 1080 \text{ m}$$

$$A = 7.06858 \text{ m}^2 \quad (d = 3 \text{ m})$$

$$\rho_\ell = 1000 \text{ kg/m}^3$$

is approximately 500 seconds.

The mass transfer parameters (K_r, n_b), relative velocity and fluid friction are assumed to be functions of void fraction and are calculated from the constitutive relations for typical bubble radii and nucleation densities.

During system charging the influx of air in the lower reservoir first increases reservoir pressure and induces an upflow in the compensation shaft. As the fluid travels up the shaft, it moves into a region of lower pressure supersaturating the solution. Because the system is supersaturated, gas dissolution occurs, which decreases the two-phase density head and increases system velocity. At approximately 100 s into the transient, the volumetric outflow of liquid exceeds the compensating influx of air and the cavern pressure begins to decrease. Figures 5.4 and 5.5 also illustrate the rapid change in pressure and velocity gradients once the compressors are turned off at t = 1000 s. Once the cavern pressure decreases to a value insufficient to compensate from the two-phase density head, frictional losses and convective acceleration forces reverse flow to occur. Reverse flow forces liquid back into the lower reservoir, which increases the lower cavern pressure and results in an oscillatory flow behavior.

During reverse flow, liquid entering the shaft from the upper reservoir is saturated at the ambient pressure and contains a much smaller

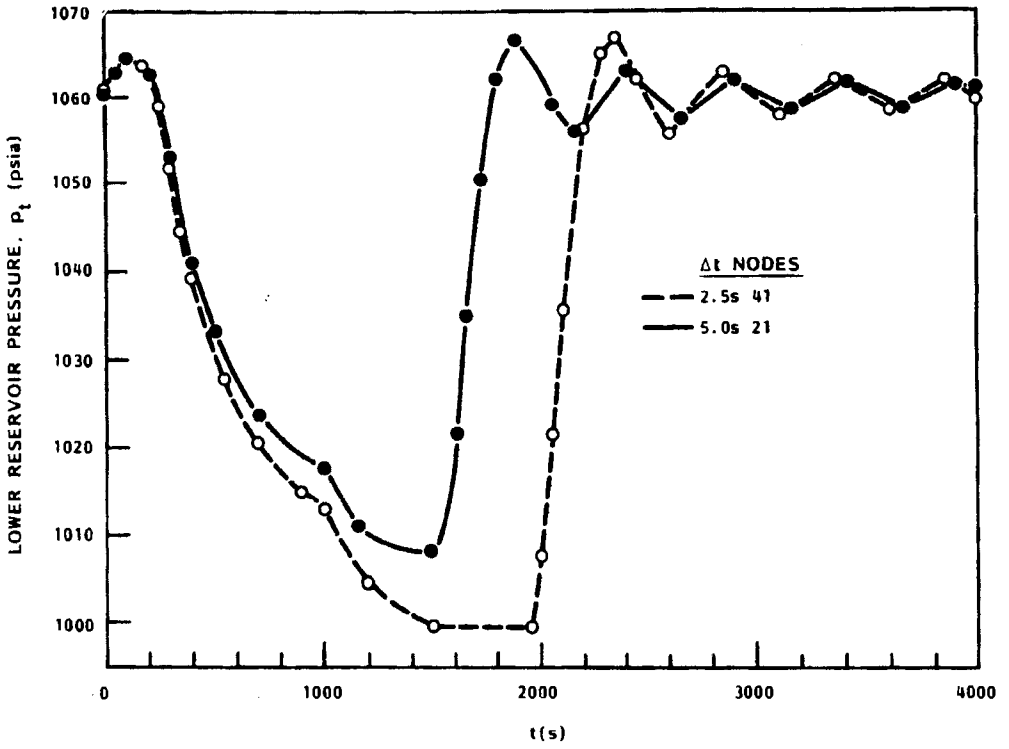

FIGURE 5.4. Lower Reservoir Pressure as a Function of Time for a Typical PEPCO CAES Startup Transient

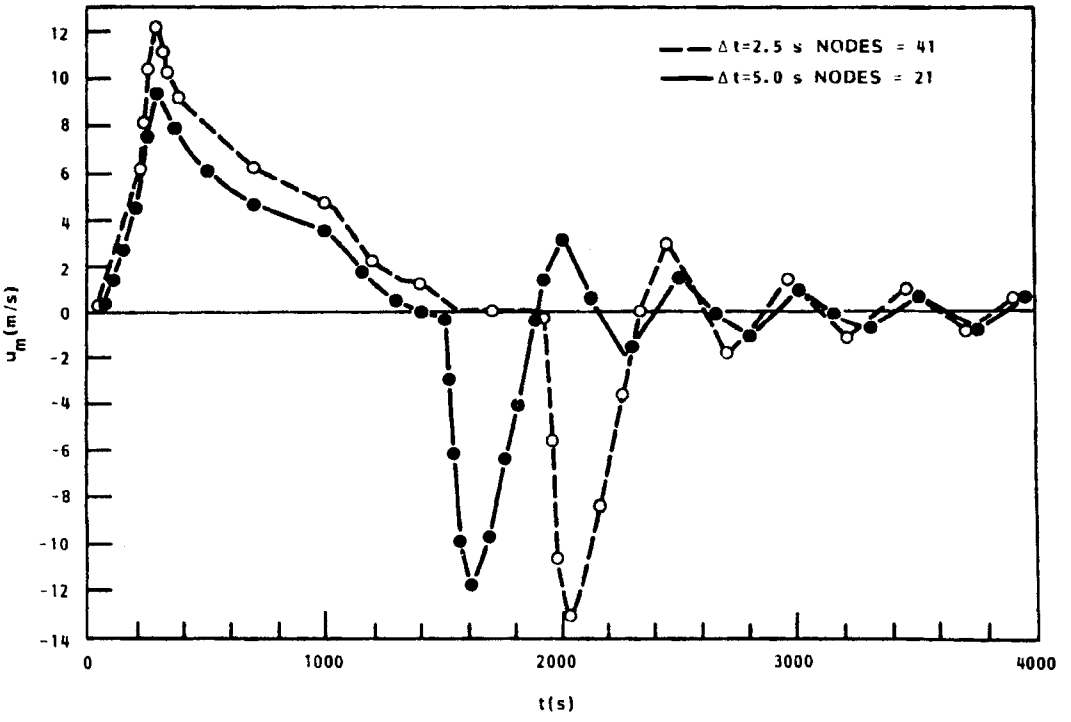

FIGURE 5.5. Exit Velocity as a Function of Time for a Typical PEPCO CAES Startup Transient

concentration of dissolved air than the high pressure lower reservoir ($\sim$1:72). Consequently, on subsequent fluid upflows, gas dissolution does not occur because the concentration pressure in the shaft remains near atmospheric (as shown in Figures 5.4, 5.5, and 5.6). This is evident by observing the fluid velocity behavior during the first flow reversal and on successive oscillations. Because the initial flow reversal reaches velocities in excess of 10 m/s, the entire compensation shaft and U-bend are replaced with liquid saturated at atmospheric pressure. On subsequent upflows, the velocities and period of oscillation are insufficient to replace the low concentration atmospheric solution with the high concentration lower reservoir solution to initiate dissolution. Consequently, the system is undersaturated for the remaining duration of transient and behaves as a spring-mass system.

Figures 5.4 and 5.5 show that the pressure and velocity period of oscillations are approximately 500 s after flow reversal. This numerical result is in excellent agreement with the period of oscillation given by Equation (88). Comparing Figures 5.4 and 5.5 also illustrates the expected pressure/velocity phase shift angle of $\pi/2$ radians. The oscillatory pressure and velocity amplitudes are shown to decrease with time because of fluid friction damping. The system is thus well behaved and will come to rest at static equilibrium.

Figure 5.6 shows some interesting characteristics of the void fraction profile. The dip in the void fraction profiles near t = 300 s is a result of the initially high saturated slug of liquid from the U-bend reaching the upper reservoir. Because this fluid slug has a higher gas concentration than the lower reservoir, dissolution is enhanced. Once the initial U-bend fluid passes through the system, the void fraction decreases as a result of the lower gas concentration level in the lower reservoir. The system velocity, however, reaches a maximum of $\sim$ 12 m/s at t = 300 s and then begins to decrease. This decrease in velocity increases the time for mass transfer to take place and allows the void fraction to approach full dissolution. Once reverse flow occurs, the exit void fraction rapidly falls to zero and remains zero throughout the transient.

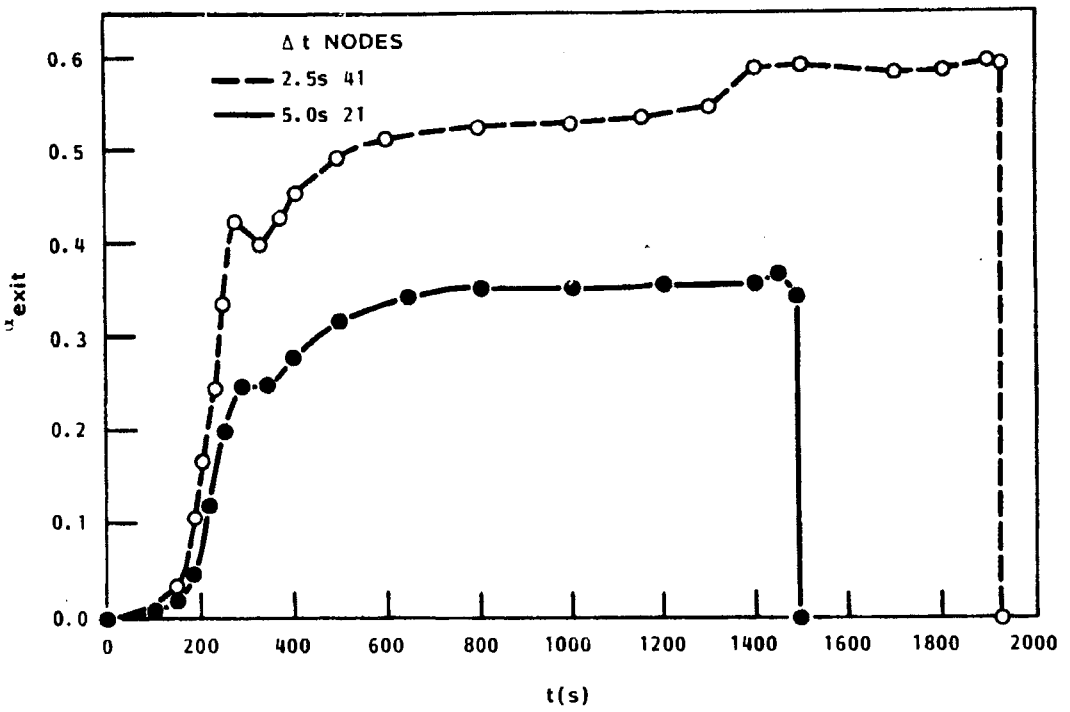

FIGURE 5.6. Exit Void Fraction as a Function of Time for a Typical PEPCO CAES Startup Transient

The effect of mesh refinement on the pressure, velocity and void fraction profiles is demonstrated in Figures 5.4 through 5.6. (Increasing the number of nodes near the exit with an axial transformation function would be a more effective and efficient method of accomplishing node refinement in areas of large void fraction and velocity spatial gradients. However, for illustration purposes, doubling the number of nodes was sufficient to demonstrate the influence of mesh size on the results.) Comparison shows that mesh refinement results in larger exit velocities and void fractions. These results were expected because of the large field gradients near the exit. Grid refinement thus enables more accurate calculation of rapidly changing spatial variables without substantial linearization. Because of the decreased two-phase density head with grid refinement, exit velocity and void fraction increases, which increased the time prior to flooding.

The results presented for this CAES design transient show the general effects gas dissolution has on the operation and dynamic response of a typical CAES system for realistic mass transfer parameters. Although these results are more investigative than quantitative, they do provide a means for evaluating two-phase dissolution flows in CAES systems. The numerical model has also demonstrated its ability to correctly predict flow oscillatory behavior.

6.0 EXPERIMENTAL ARRANGEMENT

This section documents the laboratory model arrangement and describes the tests conducted.

6.1 MODEL AND PROTOTYPE SYSTEMS

Full-size CAES installations are expected to have vertical heads on the order of 1000 meters compensation, shaft diameters on the order of 1 to 2 meters, and caverns with volumes in the millions of cubic meters. The scaling of these large size systems to laboratory models was accomplished by identifying the dimensionless numbers which characterize the features of the system to be studied. These numbers were obtained from the mathematical model of the system. The laboratory model was then designed to operate with dimensionless numbers that are within the range of those experienced by the full-scale system (Chen 1981).

The space available and practical consideration limited the experimental system to a head of 9.96 meters. Because full dissolution is expected in real CAES systems, the experimental model was designed to yield the same full-dissolution exit void fraction as a full-scale system. Large quantities of dissolved-gas release can be achieved experimentally by reducing the upper reservoir pressure, selecting a high-solubility, gas/liquid combination, supersaturating the liquid in the lower reservoir, or any combination of these. The high solubility, gas/liquid approach was chosen for this facility primarily because it was the easiest to operate and required a minimum of instrumentation.

The important nondimensional modeling parameters identified by mathematical modeling are:

1. The ratio of the liquid hydrostatic head of the compensating shaft to the atmospheric pressure, i.e., the hydrostatic head number

$$\pi_h = \rho_\ell g H / p_a \tag{89}$$

2. The gas to liquid volume ratio required to saturate the liquid in the lower reservoir, i.e., the solubility number

$$\pi_s = \Lambda \rho_\ell RT \tag{90}$$

3. Henry's constant for carbon dioxide, given by

$$\Lambda = \frac{1.83568(10^{-8})}{K} \frac{kg(gas)}{kg(liquid)N/m^2} \tag{91}$$

where K is a known function of temperature. (see Table 6.1)

4. The relative amount of gas in solution in the lower reservoir, i.e., the degree of saturation

$$\eta_1 = \frac{(P_c)_{ga}}{\rho_\ell gH} \tag{92}$$

If $\eta_1 > 1$, the lower reservoir is supersaturated. If $\eta_1 < 1$, it is undersaturated.

5. The ratio of the lower reservoir pressure to the hydrostatic pressure, i.e., the degree of pressurization

$$\eta_2 = \frac{(P_t)_{ga}}{\rho_\ell gH} \tag{93}$$

If $\eta_2 > 1$, the reservoir is overpressurized. If $\eta_2 < 1$, it is underpressurized.

6. The ratio of the friction pressure drop to the dynamic head, i.e., the friction parameter

$$\pi_f = \frac{fL}{2D} \tag{94}$$

The experimental system shown in Figure 6.1 was originally designed and constructed to model the gas-to-liquid volume ($\pi_h \times \pi_s$) of a 1000-m prototype CAES using ethyl alcohol and carbon dioxide as the working fluids. Because of costly safety equipment required for the alcohol, this

TABLE 6.1. Temperature Coefficient K for Henry's Constant for Carbon Dioxide

T	K	T	K	T	K
10	0.7915	17	0.987	24	1.20
11	0.8190	18	1.010	25	1.24
12	0.8455	19	1.040	26	1.27
13	0.8730	20	1.070	27	1.30
14	0.9010	21	1.110	28	1.34
15	0.9200	22	1.140	29	1.37
16	0.9580	23	1.170	30	1.41

9-m high system was converted to a 10-m high water and carbon dioxide system. Unfortunately, the solubility of CO_2 in water is one-fourth that of CO_2 in denatured ethyl alcohol. This reduction could have been compensated for by increasing the system height by a factor of two, but space limitations prevented that. (By way of comparison, for the 9-m alcohol/CO_2 system, $\pi_h \times \pi_s = 1.92$ while for the 10 m water/CO_2 system $\pi_h \times \pi_s = 0.9$, when both are at 20°C). With the switch to a safer working liquid means, the modified experiment actually modeled a prototype with a head of about 500 m, instead of the 1000 m originally planned.

For the equilibrium dissolution of a homogeneous flow, the void fraction can be written as

$$\alpha = \frac{\pi_h \times \pi_s \times \eta_1}{1 + \pi_h \times \pi_s \times \eta_1} \tag{95}$$

This equation shows that varying the degree of saturation, η_1, has the same effect on the void fraction as varying either the hydrostatic head or the gas-liquid solubility. The maximum pressure that may be safely applied to the windows in the reservoir is 20 psig, which limits the maximum attainable degree of saturation to 1.4. Therefore, the maximum gas-to-liquid volume that can be obtained by measuring the void fraction is 1.26, which is calculated from

$$\frac{\alpha}{1 - \alpha} = \pi_h \times \pi_s \times \eta_1 = 1.4(0.9) = 1.26 \tag{96}$$

To determine its effect on the rate of gas dissolution, five different degrees of saturation (π_h = 0.8, 0.9, 1.0, 1.1, 1.2) corresponding to two different degrees of pressurization (π_s = 1.00 and 1.02) for two ranges of particle densities (n_b = 10^8 particles/m^3, 10^9 particles/m^3) were tested.

6.2 EXPERIMENTAL SYSTEM; MEASUREMENTS

The major components of the 10-m system and their relative locations are shown in Figure 6.1. Figure 6.2 is a schematic of this system.

The epoxy-lined lower reservoir (or main tank) is mounted with its axis horizontal. Observation windows at opposite ends of the tank permit viewing the liquid level and, with proper lighting, sighting horizontally through its contents. This 240-gallon tank can accommodate approximately 190 gallons of water with an additional volume above it reserved for the charging gas and pressurization.

The U-bend and vertical compensating shaft are constructed of 76.2-mm clear cast acrylic pipe. Following the initial pipe installation it was found that roughness of the joints between pipe sections acted as nucleation sites, which generated unwanted bubbles. These sites were eliminated in the final model installation by using a special sleeve-type joint, Figure 6.3, which required machining of the pipe ends. Sealing was accomplished with the use of rubber gaskets.

To control the size of the particles in the water, a two-stage water filtering system was installed in the return pipe between the holding tank and the lower reservoir. Both stages use replaceable filters, the first a 20-micron cartridge, the second a 5-micron cartridge.

Except for the U-bend and compensating shaft, PVC piping was used throughout. The upper reservoir was made of PVC and the holding tank was stainless steel. This construction, coupled with the filtering system, allowed for close control of the system cleanliness.

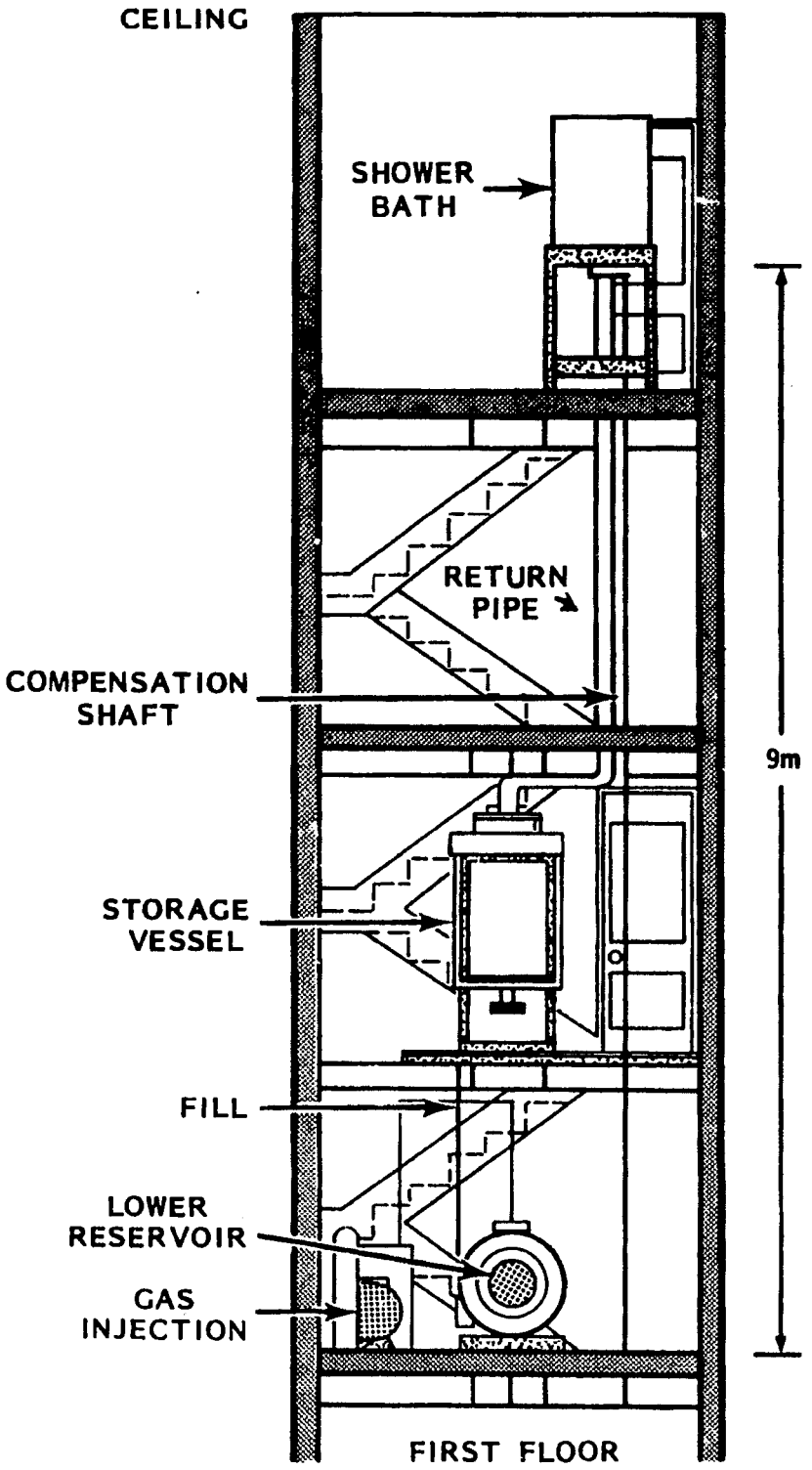

FIGURE 6.1. The Preliminary 9-m Alcohol/Carbon Dioxide System

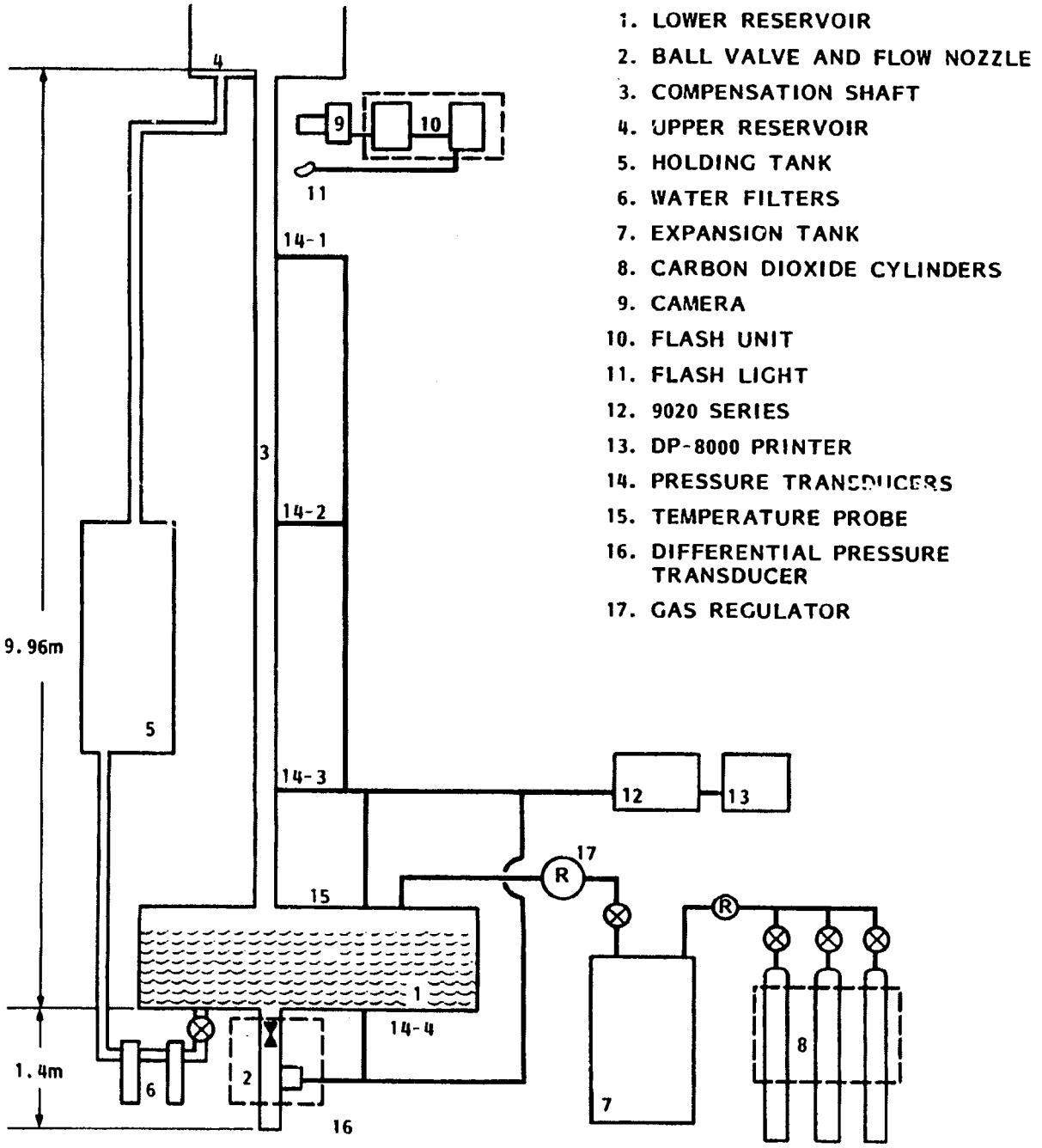

FIGURE 6.2. Rensselaer Polytechnic Institute 10-m Water/Carbon Dioxide System

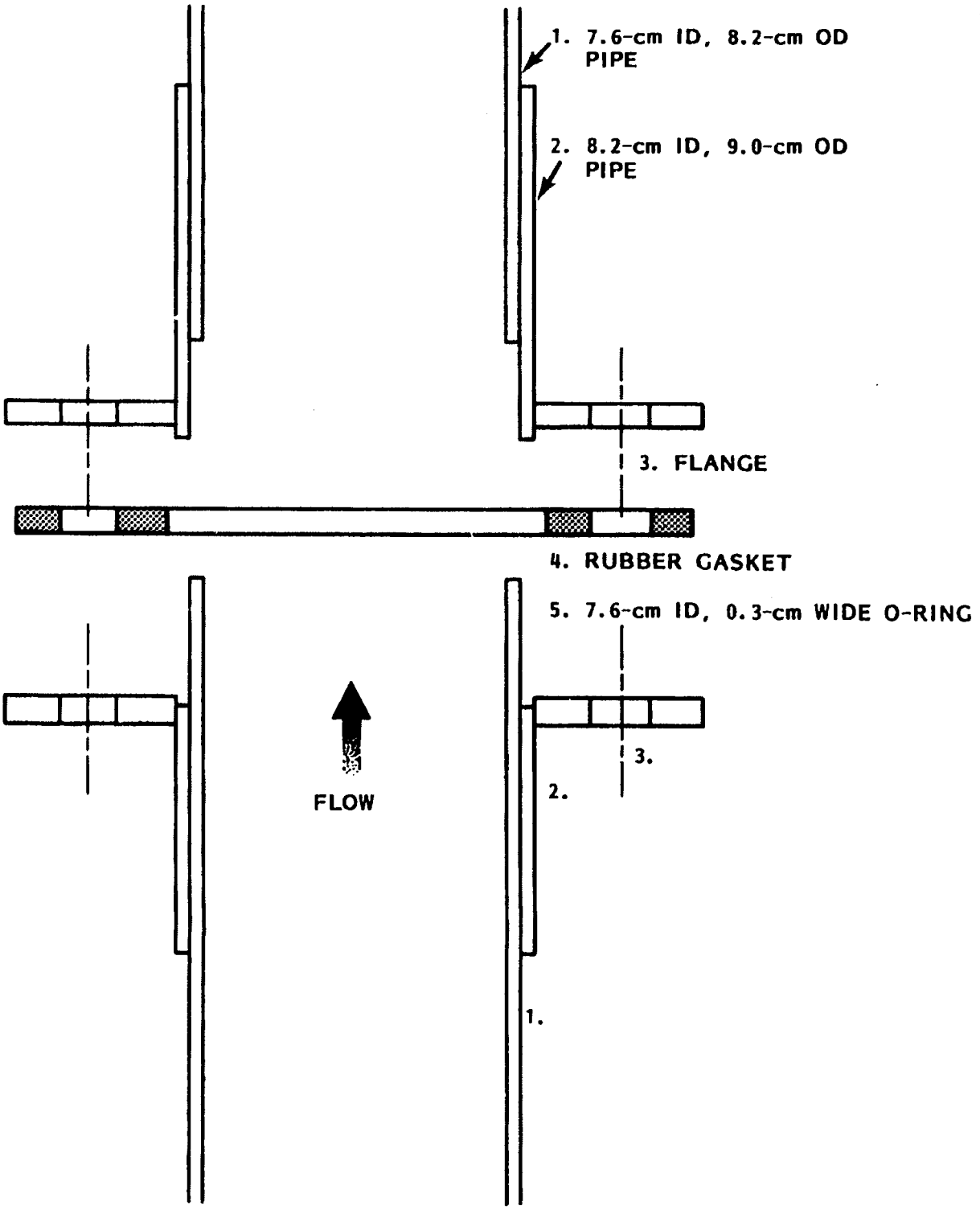

FIGURE 6.3. Sleeve-Type Joint

The U-bend is composed of a two-flanged reducer, a ball valve, and a flow nozzle with connecting piping. Based on a homogeneous, full dissolution flow model of water and CO_2, the U-bend depth required to prevent blowout was estimated to be at least 34% of the compensating shaft height, i.e., about 3.4 m. The actual depth of the installed U-bend is 1.4 m, so that a loss-of-pressure accident is theoretically possible with this system.

Although an ASME flow nozzle was installed to measure the flowrate, it was never used due to a delay in the receipt of the required differential pressure transducer. Flow rates were measured using a stop watch and a calibrated grid on the main tank.

A Daytronic 9020 modular instrument system and an Anadex DP-8000 high-speed printer were used to collect and record pressure and temperature in the experimental system. Four Kulite metal diaphragm XTM-190-25 pressure transducers, rated from 0 to 25 psig with an accuracy of $\pm$ 1% full-scale, were mounted at different positions along the compensation shaft. A YSI-703 temperature probe, with a range of -30°C to 100°C with an accuracy of $\pm$ 0.1°C was used to measure temperature. This probe was mounted on the top of the main tank to measure the gas temperature. Figure 6.4 shows the locations of the pressure transducers and temperature probe.

The void fraction was determined from photographs taken near the pipe exit. A Bronica ETRS camera with a 75-mm lens equipped with an automatic bellows was set up 1 foot below the pipe exit. By completely compressing the bellows, focusing the lens at infinity, and setting the front lens 14.2 cm from the center of the pipe, pictures 7.76 cm wide and 5.99 cm high were obtained. The flash system used to freeze the moving bubbles was a General Radio 1541 Multiflash Generator and General Radio 1539 Stroboslave. The light source was placed beside the pipe. When triggered, the light flashed toward the back of the pipe where a bright background reflected the light back through the pipe to the lers. This arrangement provided an even light distribution across the whole p cture.

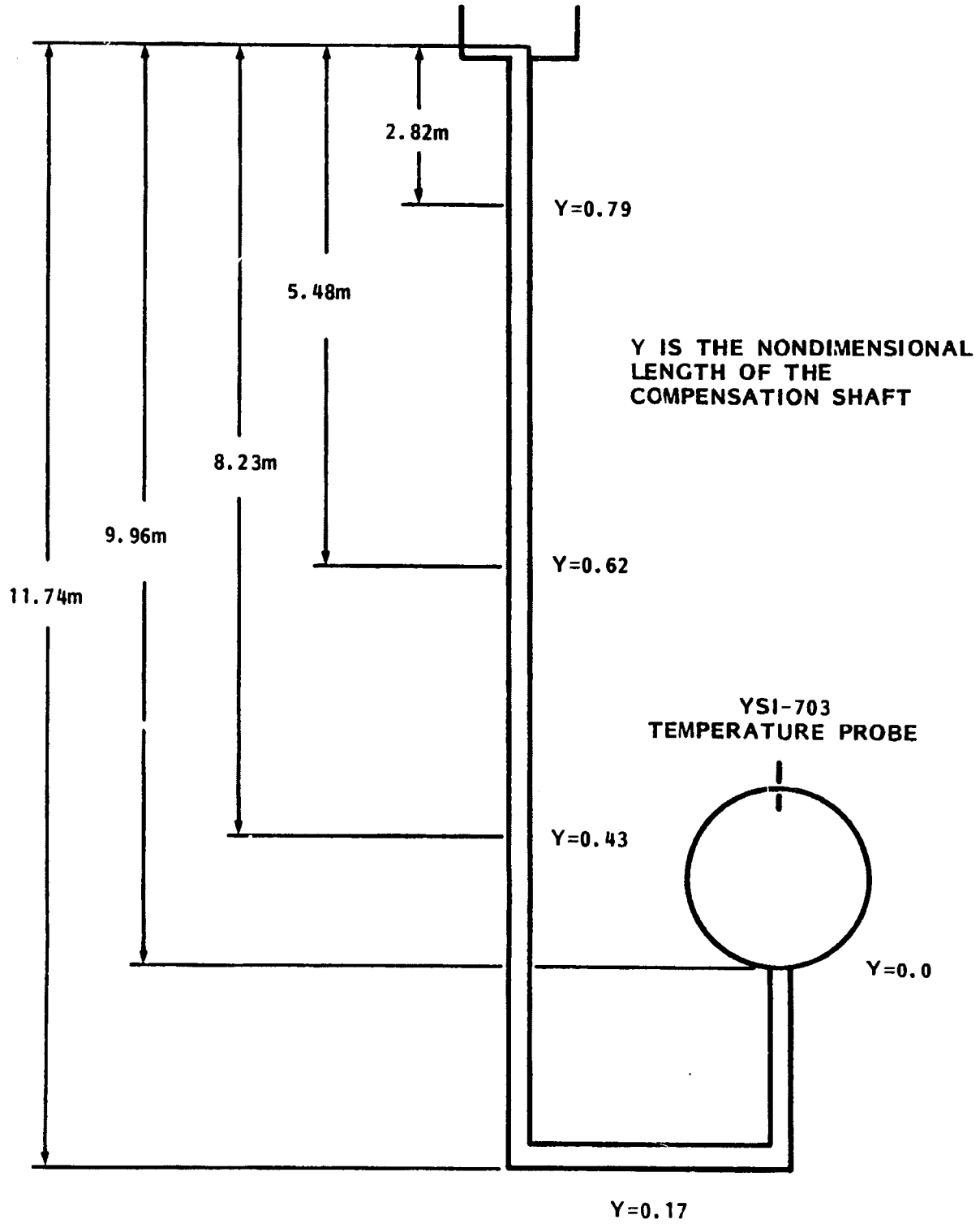

FIGURE 6.4. Transducer and Temperature Probe Locations

A method of measuring the percentage of saturation at a particular pressure was developed. Figure 6.5 shows the setup and operation of the saturation meter. Following the extraction of a sample from the lower reservoir, the sample pressure was released by opening a valve connecting the sample vessel to a plastic bag, which was initially empty and immersed in a column of water. Gentle agitation of the column was used to promote the release of gas into the plastic bag. The volume of gas evolved was measured by the displacement of the water column surrounding the bag. (A fully saturated water sample should yield 1537 cm^3 of CO_2 at 20°C.)

The basic idea was that the full dissolution gas-to-liquid volume is limited by the value of $\pi_h \times \pi_s \times \eta_1$. By collecting all of the released gas from a sample and comparing this to the theoretical gas volume, the percentage of the dissolved gas (percentage of saturation) can be calculated.

A HIAC Model PC-320 with a CMH-150 sensor was used to measure particle sizes and particle concentration in the system water. This sensor can measure particle sizes ranging from 0 to 150 microns with a concentration limit of 4000 particles/ml. Standard quartz sand, Al_2O_3, with a specific gravity of 4.0 and a size range of 0 to 30 μm was used for artificial nucleation seeding.

Unfortunately, Al_2O_3 particles are very heavy. It was found that those larger than 10 microns would settle to the bottom of the tank during the thirty minutes required to make a test run. Consequently, particle suspensions were prepared separately and allowed to settle before being introduced into the lower reservoir. Thorough dispersion of the remaining particles was accomplished by the agitation used to promote the gas dissolution process.

6.3 OPERATION

The operating procedure for each run was divided into two stages, the pre-run preparation stage and the discharge stage. During the first stage

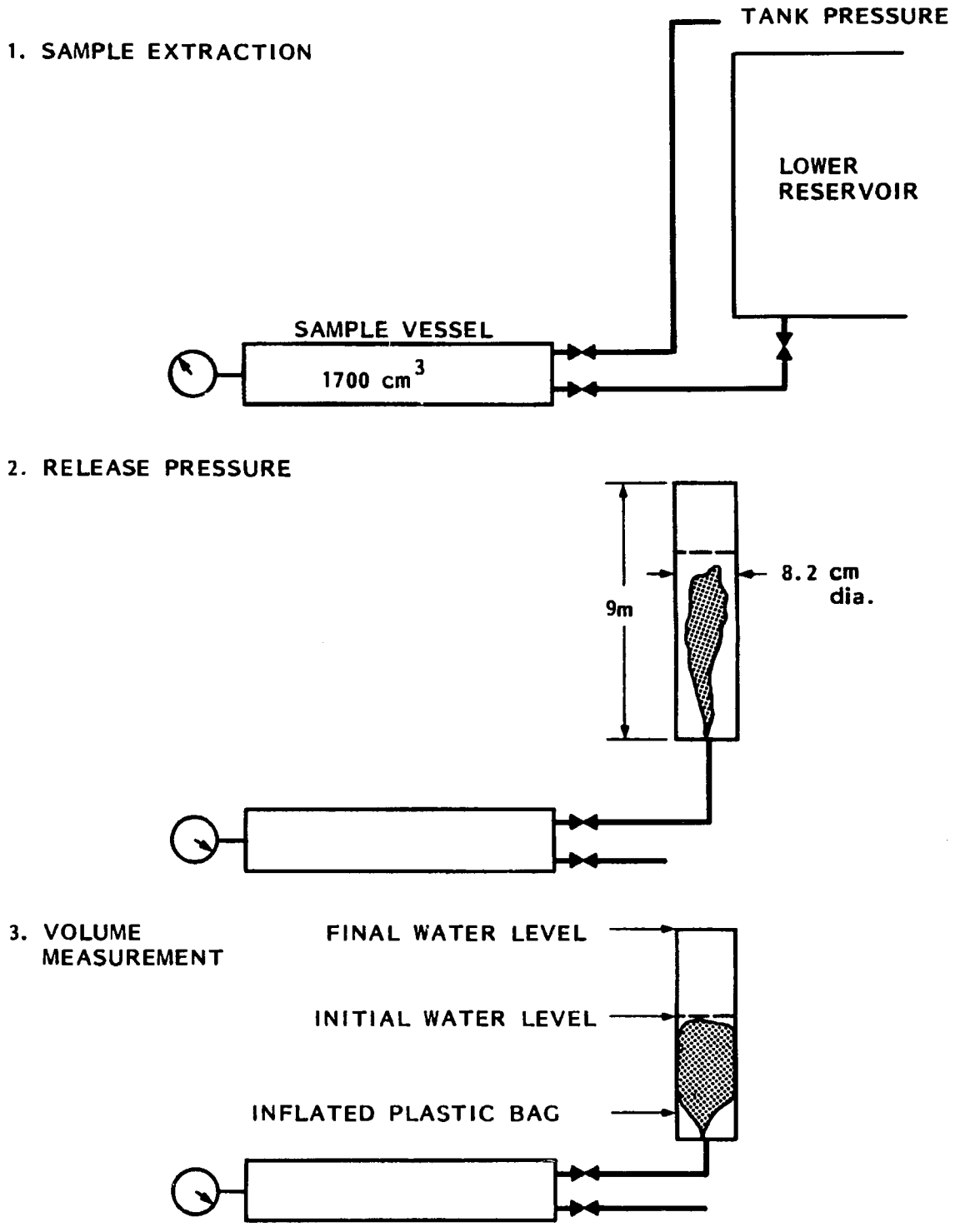

FIGURE 6.5. Saturation Meter Setup and Operation Steps

the particle count was determined, the liquid was saturated with gas, and the main tank was pressurized with gas. During the second stage the water was forced out of the main tank and up the compensation shaft, discharged into the upper reservoir at atmospheric pressure, and collected in the holding tank.

The liquid saturation process involves both pressurization and agitation. The ball valve was first opened, allowing the compensation shaft to fill with water to the water level of the main tank. The expansion tank valve is opened, allowing gas to flow into the main tank. As the main tank is pressurized, water is forced out of the tank into the compensation shaft. When the compensation shaft is full, the ball valve is closed. The pressure in the main tank is then equal to the hydrostatic head. The tank pressure is set to the desired saturation pressure and the agitation pump turned on. At the beginning of the saturating process, the pressure drops rapidly because of the high concentration difference. The gas regulator is opened wide at this stage, allowing a high gas flow rate to compensate for the high rate of gas absorption in the lower reservoir. As the pressure rises back toward the desired level, the regulator is reset to a lower flow rate, which is sufficient to keep the pressure constant. (Through experimentation, it was found that about 30 minutes were needed to fully saturate the water for all degrees of saturation.)

Following saturation, the agitation system is turned off, and the expansion tank pressurized to 0.068 MPa. The main tank pressure is then reset to the static head pressure and the ball valve opened. Pressure in the main tank is increased to, and maintained at, the desired operating pressure for that run by adjusting the regulator while monitoring the digital pressure indicator.

After approximately 17 gallons of water are discharged from the tank (the volume of water in the compensation column), bubbles form in the pipe. The location of bubble formation is dependent upon the degree of saturation. The lowest location was 9.5 m below the exit for a degree of

saturation equal to 1.2. In this case only a few bubbles with sizes less than 0.03 cm were observed. Bubbles with spherical, oblate ellipsoidal and spherical cap shapes are found in the bulk of the moving fluid.

During each run, data was collected by the data acquisition system and printed by a high-speed printer. The flow rate was measured after the tank pressure reached steady-state. A stop watch was used to record the time for every 10 gallons of water that drained from the main tank. A stop watch was also used to record the time for bubbles to travel a 0.61-m distance, from 1.22 m to 0.61 m below the pipe exit. Two or three pictures were taken during the steady-state portion of each run.

The photographs used to determine the void fraction near the shaft exit were enlarged to 24.4 x 19.2 cm. It was found that some of the bubbles near the edge of these prints were lost or distorted because of a magnifying effect. Some of these bubbles appeared to be larger than they actually were; hence, the void fraction determined photographically is slightly larger than the true value.

Distortion is a problem inherent to circular pipes. It can be avoided by mounting a rectangular, square acrylic box around the pipe, filling it with water, and photographing through it. This was not done in this preliminary study of the champagne effect because the primary objective was to explore the broad features of the phenomenon and set the stage for further detailed investigation.

High bubble density (above 5 x 10^5 bubbles/m^3) also limited the void-fraction measurements which could be obtained from the pictures. High bubble density caused the bubbles to overlap in the photographs. As a result, some bubbles were hidden by other bubbles. These hidden bubbles were not only difficult to measure, but also difficult to count.

All pictures taken were "close-up". The depth of field was shallow, although the aperture was set at the minimum position, f22. Therefore, small bubbles (radius less than 0.06 cm) were vague when they were beyond the depth of the field.

The experience gained from using this technique indicates that the photographic method can be used only when the void fraction is less than 5%, and the bubble radii are larger than 0.06 cm.

A direct comparison of the experimental results with theoretical predictions requires an accurate measurement of the saturation level in the lower reservoir. Unfortunately, the volume of gas collected by the saturation meter was never more than 50% of the expected value based on full equilibrium dissolution calculations.

The reason for the failure of the saturation meter is still unknown. The criterion established for fully saturating the lower reservoir was 30 minutes of vigorous agitation under a blanket of pressurized CO_2. It was found experimentally that the pressure in the lower reservoir would increase after the gas inlet regulator was shut off following the first 30 minutes of agitation. This was assumed to mean that agitation beyond 30 minutes forced gas to leave the already saturated solution. It is apparently much more difficult to remove gas from solution than to cause it to go into solution. Without vigorous agitation, numerous nucleation sites, and some means of removing the evolved gas, the dissolution process seems to be governed by the very slow molecular diffusion process. The ability to predict the rates of dissolution and the factors affecting them is, of course, fundamental to understanding the champagne effect. The failure of the simple device to respond as anticipated could be an indication of how little is really known about the fundamental mechanisms controlling this phenomenon.

6.4 EXPERIMENTAL RESULTS

The test program was actually performed in two stages. Exploratory tests were initially performed on the 9-m system designed to use ethyl alcohol and carbon dioxide. The qualitative results obtained with this installation were factored into the design of the subsequent 9.96-m system described in Sections 6.1, 6.2, and 6.3. Quantitative tests were then performed using water and carbon dioxide in the 9.96-m system.

The results of the exploratory tests will be reviewed first because much of what was subsequently done was motivated by the experience gained using this system.

Mindful of the potential hazards of ethyl alcohol, testing began using dilute alcohol/water mixtures and carbon dioxide. Ethanol/water ratios of 1:100 were used initially and later increased to 1:10. Very large void fractions were observed near the top of the compensating column with the more concentrated solution, so much so that the reduced head induced a noticeable increase in the flow rate. This increase was accompanied by a further increase in exit void fraction, resulting in a buoyancy-driven accelerating flow. The head in the compensating column quickly decreased to the point where it could no longer balance the main tank pressure, causing a system blowout, i.e., a simulated loss-of-pressure accident. Figure 6.6 shows the geyser produced in the upper reservoir by the blowout.

After a short period of testing, it was found that the water/alcohol mixture had become cloudy. Upon inspection of the system it was discovered that the mixture had removed much of the aluminum paint from the inside of the lower reservoir. The aluminum particles from the paint, plus rust, had contaminated the system. When the fluid was agitated to promote CO_2 absorption, these particles were also driven into suspension, clouding the mixture. It was assumed that these particles acted as nuclei for bubble formation and were responsible for the large exit void fractions.

At this point the system was disassembled. Metallic piping was replaced with plastic; the main tank was cleaned, sand-blasted, and lined with an epoxy coating. While this work was in progress, it was found that the cost of making the area safe for testing with a pure alcohol/CO_2 system was prohibitive. It was then decided to proceed with a water/CO_2 system instead. This decision led to further modifications of the system. The head was increased from 9.00 m to 9.96 m. The 25.4-mm PVC compensating pipe was replaced with 76.2-mm clear cast acrylic pipe. A two-stage

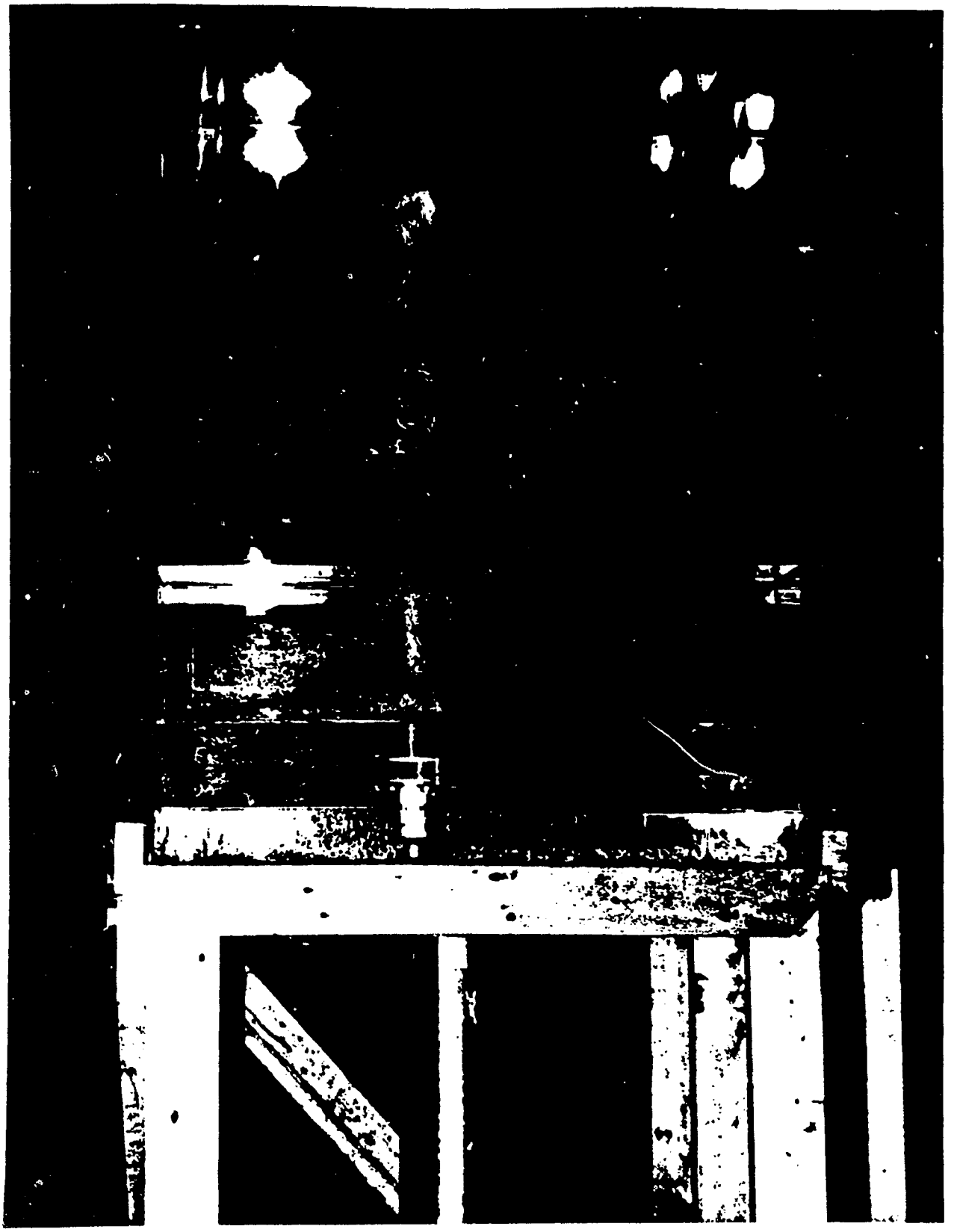

FIGURE 6.6. Geyser at Reservoir

filtering system was added, and the final instrumentation installed. The details of this final configuration have already been described in the preceding sections.

A test plan was then formulated to investigate the effects of particle seeding, as well as those of saturation (η_1) and pressurization (η_2). The quantitative results of the second stage of the test program were obtained following this plan. These are discussed in the following paragraphs.

Figure 6.7 is a plot of the exit void fraction versus inlet velocity for several degrees of saturation. The solid lines represent the predicted values obtained from the theoretical model described in Section 3. In theory, for a given inlet velocity the exit void fraction increases with increasing degree of saturation. For low inlet velocities there is a high slip ratio so that the vapor phase slips by the liquid phase, increasing the exit void fraction. As the inlet velocity increases, the slip ratio and the time for mass transfer are reduced, causing a decrease in void fraction. The experimental results conform well with these predictions.

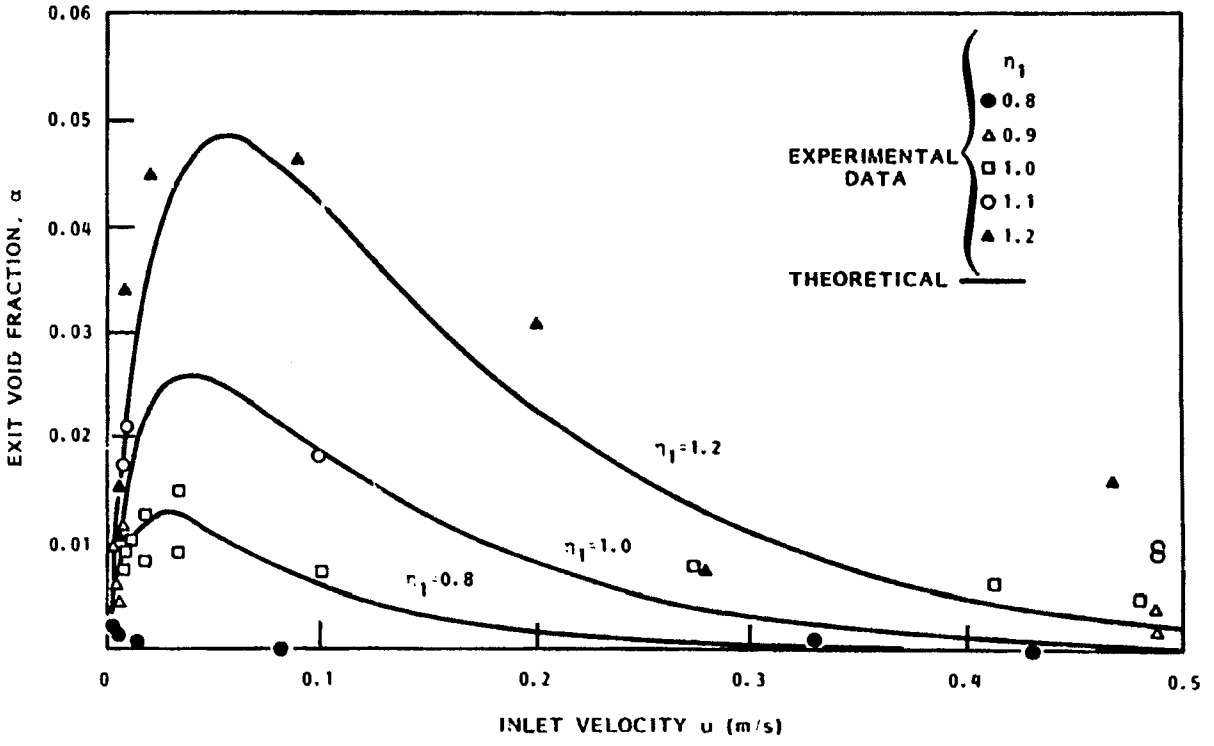

FIGURE 6.7. Comparison of Experimental and Theoretical Results in the Exit Void Fraction of Different Degrees of Saturation in a Given Inlet Velocity

Figure 6.8 shows the predicted relationship between the inlet velocity, the degree of pressurization and the degree of saturation. Although the general trend of the theory was followed, there was considerable scatter in the data. This can be attributed to the relatively low sensitivity of the pressure transducers, which was 1.7 kPa full-scale.

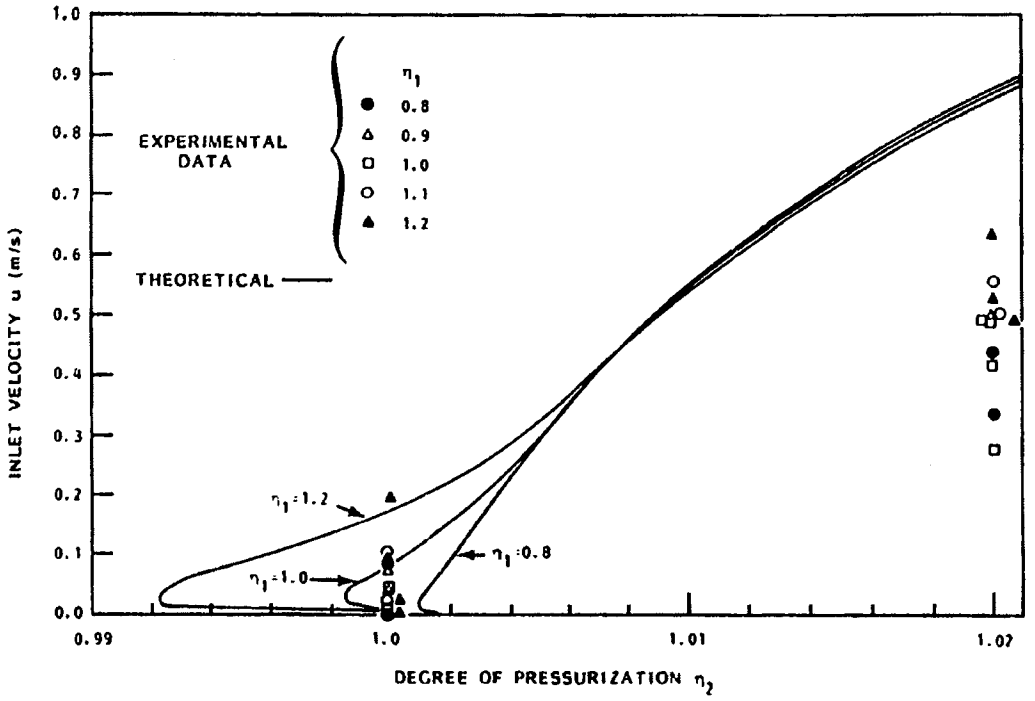

FIGURE 6.8. Comparison of the Experimental and Theoretical Result for Inlet Velocity as a Function of Degree of Pressurization and Degrees of Saturation

Flow rates lower than those theoretically predicated were never observed in the experiment. Flow was observed to stop immediately after the pressure dropped to the hydrostatic head pressure even in high saturation, low pressurization cases.

Figure 6.9 is a plot of bubble density versus seeding particle density for several degrees of saturation and pressurization. Theoretically, bubble density should increase with increasing seeding particle density. However, the test results revealed a considerable amount of scattered data

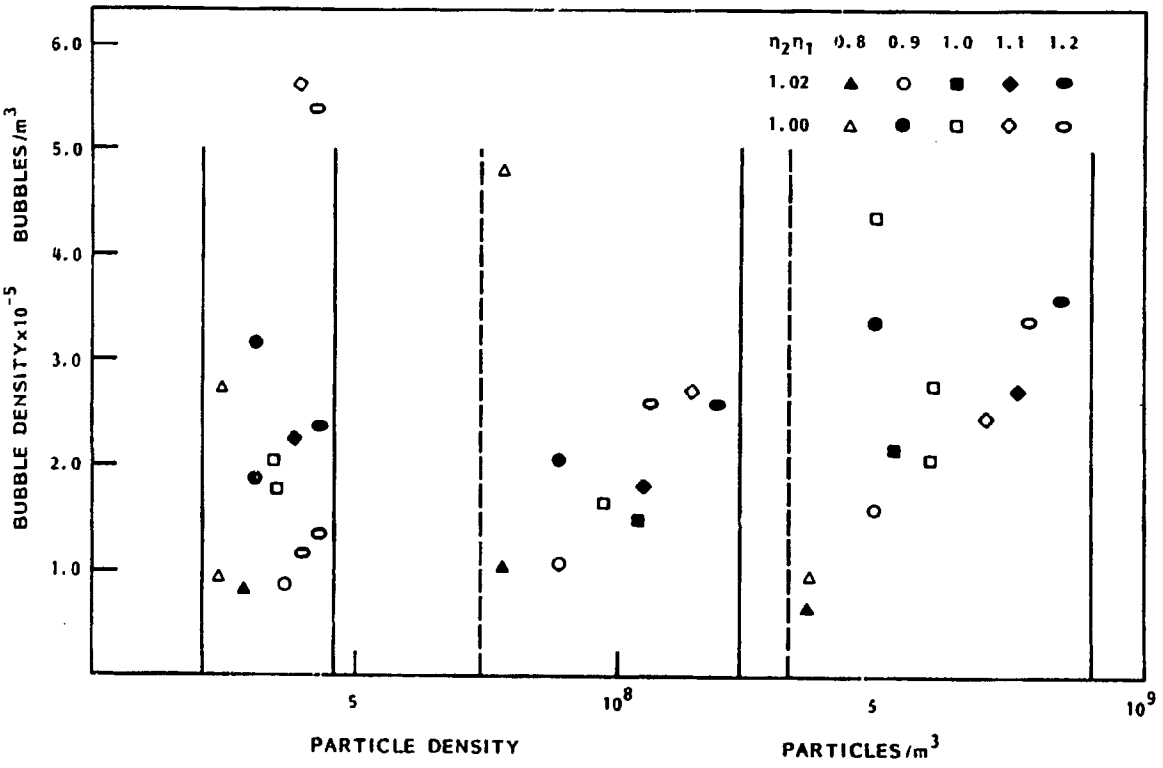

FIGURE 6.9. Bubble Density Versus Particle Density for Fixed Degree of Pressurization and Fixed Degree of Saturation

and no clear trend. There are thought to be two possible causes for this scatter. First, there may have been inadequate time for bubble development. Tests made under identical conditions did not always produce the same results. The bubble radius and bubble density for runs with the same degrees of saturation and pressurization, and the same quantity of seeding particles, often differed by as much as a factor of three. Runs made with water that had been saturated several days earlier produced considerably more bubbles than those run with newly saturated water. Second, the seeding particles may have been too small. Ninety-five percent of the particles used were under 10 microns in diameter. The equilibrium bubble radius for the water/carbon dioxide system tested is thought to be on the order of 1 micron. If the possible nucleation sites on the surfaces of the particles were not large enough to support a bubble of this size, then bubble development would be inhibited.

The test results to this point can be summarized as follows:

1. The predicted interdependence of u, α, n_1, and n_2 was found to be in substantial agreement with the trend of the test results over the limited range tested.
2. The effect of particle seeding appeared to be less dramatic than had been anticipated. No discernible trend could be identified.

A second sequence of tests was initiated to determine whether the proposed explanations for the erratic particle seeding results were correct.

The first of these tests was designed to isolate the effect of degree of saturation and degree of pressurization on bubble size and bubble density in the absence of seeding particles. Four tests were made with n_1 ranging from 1.02 to 1.06 for n_2 values of 1.02 and 1.04. Each of these runs was made with fresh water in a clean system. The results revealed no large differences in bubble size or density.

A second set of tests was performed to determine if time or the type of particles was an important factor in bubble development. Each test run was made using the same operational parameters, i.e., with degree of saturation and the flow rate arbitrarily set at 1.07 and 25 liters per minute, respectively. The water, however, was either newly saturated or saturated and allowed to remain idle at 104 kPa for specified periods of time (0, 0.5, 1.5, 6 and 18 hours). The quantity of seeding particles was kept the same for all similar runs. Tests runs were made with clean tap water, with tap water and powdered iron, and with tap water and ordinary table salt.

Newly saturated clean tap water was run as a baseline for these tests. It produced relatively few bubbles in the top 3 m of the compensation column. The bubble radius was approximately 0.625 mm. The flow was very steady and produced an exit head of 8 mm above the top of the column.

When this clean water was allowed to remain saturated for a period of time, the results were somewhat different. The photographs in Figure 6.10 show the bubble development over time. Bubble size and density increase dramatically over the 24-hour period. The maximum average bubble radius was 2.525 mm. Bubble formation began 3 m below the top of the column when the water was saturated for 1.5 hours and 5 m below when it was saturated 12 hours. The flow was, at times, erratic and produced a maximum exit head of 12 mm after 24 hours. From these tests it was estimated that bubble development reached equilibrium after 18 hours.

Following the clean water tests, the system was cleaned and refilled with fresh tap water and 100 ml of rusty powdered iron (iron oxide). This system, when newly saturated, produced much larger and many more bubbles than the comparable runs in the clean water tests. The bubble radius was 2.290 mm for the newly saturated runs. The bubbles would occasionally move in small "packs" of larger bubbles, but this was not found to be repeatable in all similar runs. The exit head for this run was 10 mm.

When the water/powered iron solution was allowed to remain saturated for a period of time, the results were very different. The bubble radius and bubble density increased over the 24-hour period and the last meter of the compensation column was frothy white with bubbles. The bubble radius increased from 2.290 mm to 3.160 mm in the first 18 hours, and remained constant. Thereafter, bubble formation began 7 m below the top of the column. The flow of bubbles was fast and steady, producing a maximum exit head of 15 mm.

Another 100 mℓ of powdered iron was then added to this already saturated solution and the system was rerun immediately. This produced no noticeable change in bubble radius or density over the previous run.

Following the tests with powdered iron, the system was again cleaned and refilled with fresh tap water. In the following runs, 500 mℓ of non-iodized table salt was used instead of powdered iron (using less than 500 mℓ produced a less vigorous result). The results from these tests were very similar to those for powdered iron, as indicated in the photographs in

Clean Water - Newly Saturated

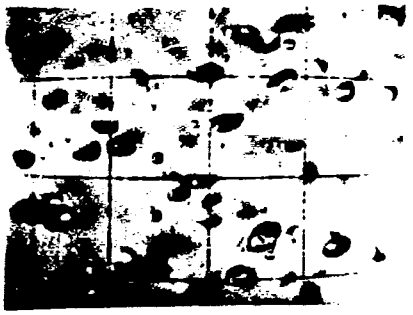

Salt Particles - Newly Saturated

Clean Water - 35 Min Elapsed Time

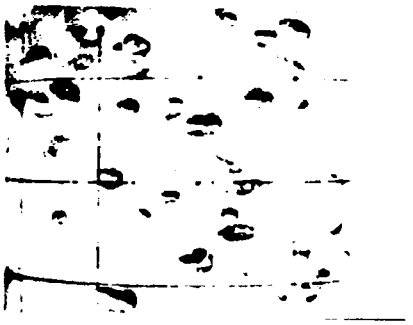

Salt Particles - 40 Min Elapsed Time

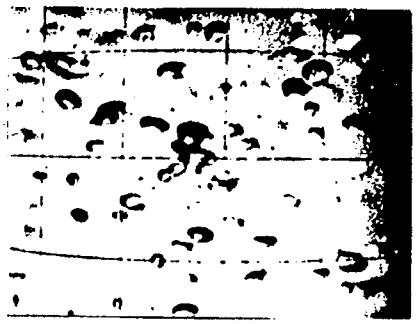

Clean Water - 1.5 Hr Elapsed Time

Salt Particles - 1.5 Hr Elapsed Time

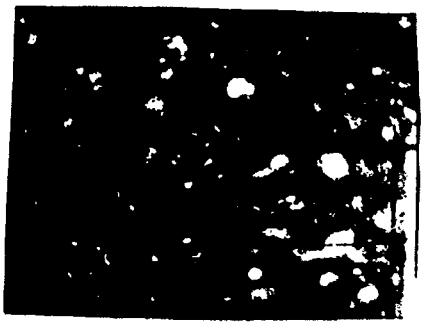

Clean Water - 24 Hrs Elapsed Time

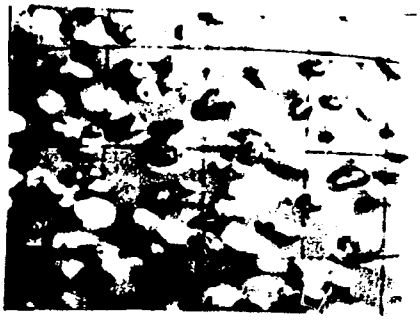

Salt Particles - 1.8 Hr Elapsed Time

FIGURE 6.10. Bubble Development Over Time

Figure 6.10. Several additional tests were made with larger quantities of salt. Salt particles were added in 250 mℓ amounts from 500 to 1500 mℓ, with a separate test run at each concentration. The results showed increases in bubble density with each addition of salt up to 1000 mℓ and little change for concentrations above that level. This is probably because the number of bubbles that can be identified with the existing instrumentation is limited. Powdered iron (reduced by hydrogen) and ordinary table salt particles were chosen because previous experience revealed their potential as active nucleation sites. The powdered iron particles were obtained from Fisher Scientific. These particles were very fine, their texture very similar to that of talcum powder.

An electron microscope was used to determine the size and shape of the powdered iron particles. Figure 6.11a is an electron micrograph of a field of approximately 150 of these particles (magnification 200x). The particles range in size from 10 microns to 90 microns, with the majority of particles in the 20- to 40-micron range. As can be seen, the shape and size of each particle is unique. The surfaces are very irregular and the edges extremely rough. Virtually all the particles contain several holes, similar to those in Figure 6.11b (magnification 1000x/5000x). These holes average 1 to 4 microns in diameter. A back-scattering micrograph (not shown) was taken to view the particles in a simulated three-dimensional perspective. This perspective showed the particles to be very similar in shape to ocean coral, their surfaces covered with many cracks and crevices 5 to 50 microns in size. All of these surface imperfections (holes, cracks and crevices) could act as potential nucleation sites for bubble formation.

When viewed under a high-powered light microscope at low magnification (50x), the salt particles appeared to be cubical with well-defined edges. The particles ranged in size from 100 microns to 500 microns, with the majority of particles in the 300- to 400-micron range. However, under high magnification (1000x), the particles were found to be rough at the edges, irregular on the surfaces, and approximately cubical in form. The individual surfaces of each particle were completely covered with small

(a) 200 X

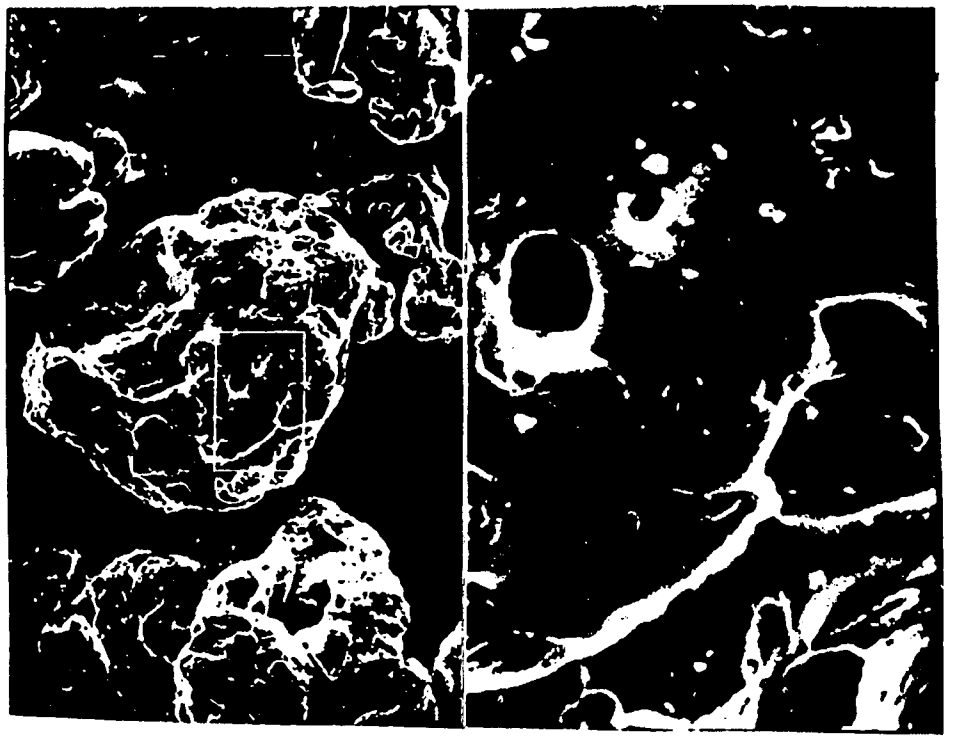

(b) 1000 X/5000 X

FIGURE 6.11. Electron Micrographs of Powdered Iron

holes 5 to 20 microns in diameter. These holes did not appear to form any particular pattern but rather were randomly distributed. Again, these holes and rough surfaces could act as potential nucleation sites for bubble formation.

REFERENCES

Burden, R. L., J. D. Faires, and A. C. Reynolds. 1978. Numerical Analysis. Prindle, Weber and Schmidt, Boston, Massachusetts.

Calderbank, P. H., and M. B. Moo-Young. 1961. "The Continuous Phase Heat and Mass-Transfer Properties of Dispersions." Chemical Engineering Science. 16:39-54.

Chen, P. V. 1981. The Preliminary Experimental Results of Modeling the Champagne Effect in a Hydraulically Compensated Compressed Air Storage System. Master's Thesis, Rensselaer Polytechnic Institute, Troy, New York.

Emmerich, W., R. Battino, and R. J. Wilcock. 1976. "Low-Pressure Solubility of Gases in Liquid Water." Chemical Reviews. 77(2):219-262.

Giramonti, A. J., W. A. Blecher, and E. B. Smith. 1982. "Simulation of the Champagne Effect in CAES Power Plants." In Proceedings, AIAA/EPRI International Conference on Underground Pumped Hydro and Compressed Air Energy Storage, ed. A. J. Giramonti, pp. 195-201. American Institute of Aeronautics and Astronautics, New York, New York.

Harlow, F. H., and A. A. Amsden. 1971. "A Numerical Fluid Dynamics Calculation Method for all Flow Speeds." J. Computational Physics. 8:197-213.

Harlow, F. H., and A. A. Amsden. 1975. "Numerical Calculation of Multiphase Fluid Flow." J. Computational Physics. 17:19-52.

Herringe, R. A., and M. R. Davis. 1978. "Flow Structure and Distribution Effects in Gas-Liquid Mixture Flows." Int. J. Multiphase Flow. 4:461-486.

Kays, W. M. 1966. Convective Heat and Mass Transfer. McGraw-Hill, New York, New York.

Kruis, A. 1976. "Gleichgewicht der Absorption von Gasen in Flüssigkeiten." (H. Hansen, ed.), Landolt-Bornstein Encyclopedia. Part 4, Volume IVc1, Springer Verlag, Berlin, Germany.

Larsen, I., and D. Norén. 1973. "Hydraulics of Compressed Air Power Plants." Paper presented at Third Conference on Compressed Gas Economy, 1973, Budapest.

Liles, D. R., and W. H. Reed. 1978. "A Semi-Implicit Method for Two-Phase Fluid Dynamics." J. Computational Physics. 26:390-407.

McAdams, W. H., W. K. Woods, and L. C. Heroman. 1942. "Vaporization Inside Horizontal Tubes: II. Benzene-Oil Mixtures." Trans. AIME. 64:193-200.

McMonagle, C. A., and D. S. Rowe. 1980. Analytical Modeling of a Hydraulically Compensated Compressed Air Energy Storage System. Rowe and Associates, Bellevue, Washington.

Meyer, B. R. 1981. Multiphase Dissolution Flows. Ph.D. Thesis, Rensselaer Polytechnic Institute, Troy, New York.

Pellin, J. 1982. "High Pressure Test Facility for Resolution of the Champagne Effect." In Proceedings, AIAA/EPRI International Conference on Underground Pumped Hydro and Compressed Air Energy Storage, ed. A. J. Giramonti, pp. 202-210. American Institute of Aeronautics and Astronautics, New York, New York.

Powell, R. J. 1972. "Solubility of 16 Gases in $(C_4F_9)_3$ N and CS_2." J. Chem. and Eng. Data. 17(3):302-303.

Ramshaw, J. D., and J. A. Trapp. 1976. "A Numerical Technique for Low-Speed Homogeneous Two-Phase Flow with Sharp Interfaces." J. Computational Physics. 21:438-453.

Rowe, D. S., and C. A. McMonagle. 1982. "Analytical Modeling of the Champagne Effect in Hydraulically Compensated CAES Reservoirs." In Proceedings, AIAA/EPRI International Conference on Underground Pumped Hydro and Compressed Air Energy Storage, ed. A. J. Giramonti, pp. 191-194. American Institute of Aeronautics and Astronautics, New York, New York.

Ruzich, R. R., and J. Miller. 1982. "The First U.S. CAES Plant - A Review." In Proceedings, AIAA/EPRI International Conference on Underground Pumped Hydro and Compressed Air Energy Storage, ed. A. J. Giramonti, pp. 102-109. American Institute of Aeronautics and Astronautics, New York, New York.

Sawa, H. 1975. Mass Transfer from a Slightly Soluble Gas Bubble in Turbulent Flow. Ph.D. Thesis, University of Washington, Seattle, Washington.

Stewart, H. B. 1979. "Calculation of Transient Boiling Flow in Channels." J. Computational Physics. 30:61-75.

Vann, R. D., and M. D. Freezor. 1982. "An Experimental Model of Bubble Formation in CAES Plants." In Proceedings, AIAA/EPRI International Conference on Underground Pumped Hydro and Compressed Air Energy Storage, ed. A. J. Giramonti, pp. 211-214. American Institute of Aeronautics and Astronautics, New York, New York.

Willett, D. C., and E. D. Shippey. 1980. Preliminary Design and Study of Underground Pumped Hydro and Compressed Air Energy Storage in Hard Rock. Acres American, Inc., Buffalo, New York.

BIBLIOGRAPHY

Electric Power Research Institute. 1979. "Eighty Atmospheres in Reserve." EPRI Journal. April 1979, pp. 14-18.

Farquhar, O. C. 1982. Geotechnical Basis for Underground Energy Storage in Hard Rock. EPRI EM-2260, Electric Power Research Institute, Palo Alto, California.

Giramonti, A. J. ed. 1982. International Conference on Underground Pumped Hydro and Compressed Air Energy Storage. American Institute of Aeronautics and Astronautics, New York, New York.

DISTRIBUTION

No of Copies

OFFSITE

US Department of Energy
Attn: J. Brogan
Office of Energy Systems Res.
Forrestal Bldg, CE-141 5E-052
Washington, DC 20585

US Department of Energy
Attn: R. A. Dunlop
Div. of Electric Energy Sys.
12 & Pennsylvania
Washington, DC 20585

US Department of Energy
Attn: I. Gyuk
Office of Energy Systems Res.
Forrestal Bldg, CE-141 5E-052
Washington, DC 20585

US Department of Energy
Attn: R. Shivers
Office of Energy Systems Res.
Forrestal Bldg, CE-141 5E-052
Washington, DC 20585

US Department of Energy
Attn: Director, Policy and Planning
Office of Conservation and Solar Applications
Washington, DC 20545

27 DOE Technical Information Center

Acres American, Inc.
Attn: C. Driggs
The Clark Building
Suite 329
Columbia, MD 21044

No of Copies

Acres American, Inc.
Attn: D. Willett
Liberty Bank Building
Main at Court
Buffalo, NY 14202

T. L. Brekke
1847 Yosemite Road
Berkeley, CA 94707

Central Illinois Public Service Co.
Attn: A. H. Warnke
Vice President Power Supply
607 East Adams Street
Springfield, IL 62701

Commonwealth Edison Co.
Attn: T. J. Maiman
Sta. Mech. Engr. Dept. Mgr.
36 FN West
PO Box 767
Chicago, IL 60690

Electric Power Research Inst.
Attn: J. Birk
3412 Hillview Avenue
PO Box 10412
Palo Alto, CA 94303

Electric Power Research Inst.
Attn: R. B. Schainker
3412 Hillview Avenue
PO Box 10412
Palo Alto, CA 94303

FluiDyne Engineering Corp.
Attn: L. Marksberry
5900 Olson Memorial Highway
Minneapolis, MN 55422

No of
Copies

Harza Engineering Co.
Attn: A. H. Barber
Director of Marketing
150 S. Wacker Drive
Chicago, IL 60606

Michael J. Hobson
PO Box 820
Columbia, MD 21044

Illinois Power Company
Attn: G. E. Huck
Manager of Planning
500 South 27th St.
Decatur, IL 62525

Lawrence Livermore Laboratory
Attn: Jesse Yow
PO Box 808
Mail Stop L-202
Livermore, CA 94550

Lawrence Livermore Laboratory
Attn: Tech. Info. Dept, L-3
University of California
PO Box 808
Livermore, CA 94550

Middle South Services
Attn: L. A. Wilson
Advanced Energy Program
Section
Box 6100
New Orleans, LA 70161

Office of Congressman
Sid Morrison
Attn: Kevin Billings,
Legislative Asst.
1330 Longworth Bldg.
Washington, DC 20515

No of
Copies

Potomac Electric Power Co.
Attn: P. E. Schaub
1900 Pennsylvania Ave
Washington, DC 20006

Public Service of Indiana
Attn: T. W. McCafferty
1000 E. Main Street
Plainfield, IN 46168

20 Rensselaer Polytechnic Inst.
Attn: P. Thompson
Dept. of Mechanical Eng.
Troy, NY 12181

Rowe and Associates
14400 Bellevue-Redmond Road
Suite 208
Bellevue, WA 98007

Sandia Laboratories
Technical Library Div. 3141
Albuquerque, NM 87185

Sandia Laboratories
Attn: William G. Wilson
PO Box 969
Organization 8453
Livermore, CA 94550

Sandia Laboratories
Attn: R. O. Woods
Organization 4715
Albuquerque, NM 87115

Sargent and Lundy Engineers
Attn: W. C. Walke
Project Manager
55 East Monroe Street
Chicago, IL 60603

No of
Copies

Tennessee Valley Authority
Attn: A. Betbeze
1150 Chestnut, Tower 2
Chattanooga, TN 37401

Tennessee Valley Authority
Energy Research Section
1360 Commerce Union Bank
Bldg.
Chattanooga, TN 37401

Tennessee Valley Authority
Attn: William Waldrop
Asst. Branch Chief
Water Systems Develop. Branch
Division of Water Management
PO Drawer E
Norris, TN 37828

TRW Energy Systems Group
Attn: E. Berman
Technical Library
7600 Colshire Drive
McLean, VA 22101

Union Electric Co.
Attn: H. C. Allen
Vice President
Research & Development
PO Box 149
St. Louis, MO 63166

United Engrs. & Constructors
Attn: A. Karalis
30 South 17th Street
Philadelphia, PA 19101

United Technologies Research
Center
Attn: A. Giramonti
Silver Lane
East Hartford, CT 06108

No of
Copies

University of Massachusetts
Attn: O. C. Farquhar
Dept. of Geology & Geography
Morrill Science Center
Amherst, MA 01003

University of Michigan
Attn: D. L. Katz
Dept. of Chemical Engineering
2042 E. Engr. Bldg.
Ann Arbor, MI 48109

US Department of Interior
Attn: Natural Resources
Library, Lucy Howton
Serials Branch (G/E)
Washington, DC 20240

Westinghouse R&D
Attn: D. L. Ayers
1319 Beulah Road
Pittsburg, PA 15235

FOREIGN

J. Pellin
Societe Electrique de l'our
2 Rue d'Aspect
Luxembourg, France

ONSITE

DOE Richland Operations Off.

H. E. Ransom/D. R. Segna

30 Pacific Northwest Laboratory

R. D. Allen
T. J. Doherty
R. L. Erikson
L. D. Kannberg (20)
Technical Information (5)
Publishing Coordination (2)